

¹
² Susceptible host dynamics explain pathogen resilience to
³ perturbations

⁴
⁵ Sang Woo Park, . . . , Bryan T. Grenfell, Sarah Cobey

⁶ Abstract

⁷ Major priority for epidemiological research in the time of anthropogenic change is un-
⁸ derstanding how infectious disease dynamics respond to perturbations. Interventions
⁹ to slow the spread of SARS-CoV-2 significantly disrupted the transmission of other
¹⁰ human pathogens. As interventions lifted, whether and when respiratory pathogens
¹¹ would eventually return to their pre-pandemic dynamics remains to be answered. We
¹² develop a framework for estimating pathogen resilience based on how fast epidemic
¹³ patterns return to their pre-pandemic, endemic dynamics. Our analysis suggests
¹⁴ that some pathogens may have settled to endemic cycles that are different from their
¹⁵ pre-pandemic patterns. Finally, we show that the replenishment rate of the suscep-
¹⁶ tible pool is a key determinant of pathogen resilience. Our framework offers a novel
¹⁷ perspective to characterizing the dynamics of endemic pathogens and their responses
¹⁸ to SARS-CoV-2 interventions. **[SWP: Need to emphasize broader implications.]**

19 Non-pharmaceutical interventions (NPIs) to slow the spread of SARS-CoV-2 disrupted
 20 the transmission of other human respiratory pathogens, adding uncertainties
 21 to their future epidemic dynamics and the overall public health burden [1]. As
 22 NPIs lifted, large heterogeneities in outbreak dynamics were observed across different
 23 pathogens in different countries, with some pathogens exhibiting earlier resurgences
 24 than others [2, 3, 4]. Heterogeneities in the overall reduction in transmission and the
 25 timing of re-emergence likely reflect differences in NPI patterns, pathogen character-
 26 istics, immigration/importation from other countries, and pre-pandemic pathogen
 27 dynamics [5]. Therefore, comparing the differential impact of the pandemic pertur-
 28 bations across pathogens can provide unique opportunities to learn about underlying
 29 pathogen characteristics, such as their transmissibility or duration of immunity, from
 30 heterogeneities in re-emergence patterns [6].

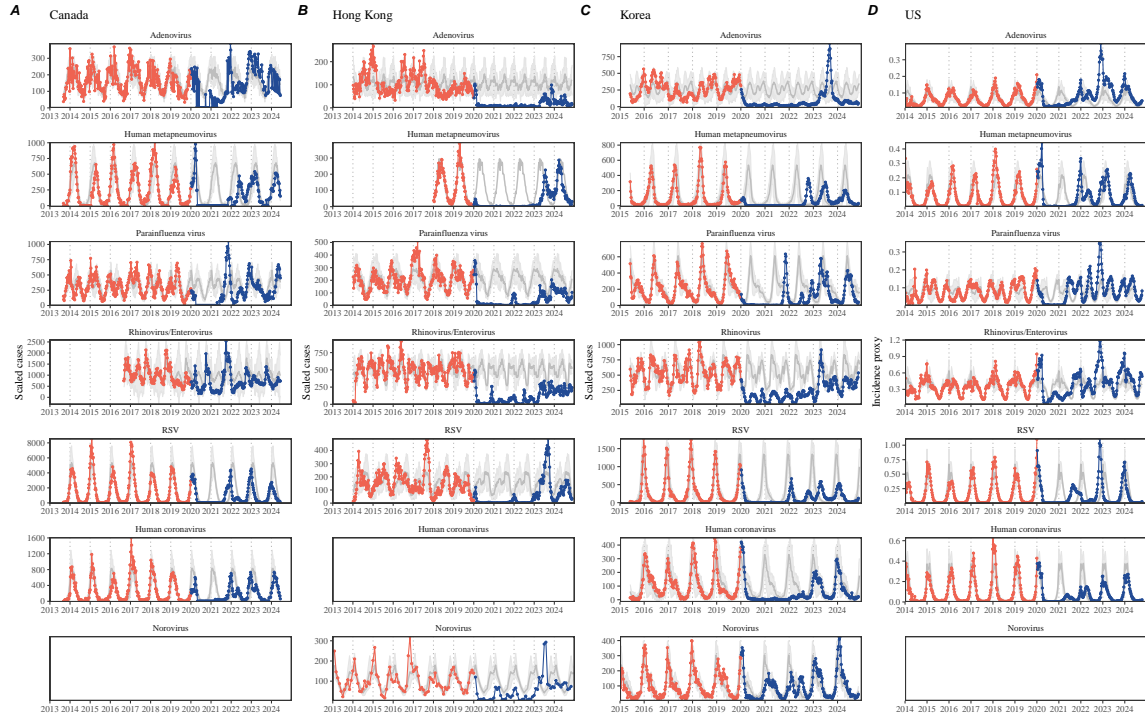


Figure 1: Observed heterogeneity in responses to pandemic perturbations across respiratory pathogens and norovirus in (A) Canada, (B) Hong Kong, (C) Korea, and (D) US. Red points and lines represent data before 2020. Blue points and lines represent data since 2020. Gray lines and shaded regions represent the mean seasonal patterns and corresponding 95% confidence intervals around the mean. Mean seasonal patterns were calculated by aggregating cases before 2020 into 52 weekly bins and taking the average in each week. Cases were scaled to account for changes in testing patterns (Materials and Methods).

31 Even though more than five years have passed since the emergence of SARS-CoV-
 32 2, we still observe persistent changes in pathogen dynamics following the pandemic

33 perturbations: for example, compared to pre-pandemic, seasonal patterns, human
34 metapneumovirus in Korea seem to circulate at lower levels, whereas RSV in Ko-
35 rea seem to exhibit different seasonality (Figure 1). These observations suggest a
36 possibility for a fundamental change in pathogen dynamics following the pandemic
37 perturbations, which can be driven by permanent shift in either human behavior
38 or population-level immunity [7, 8]. The possibility of a long-lasting impact of the
39 pandemic perturbations pose an important question for future infectious disease dy-
40 namics: can we predict whether and when other respiratory pathogens will eventually
41 return to their pre-pandemic dynamics? *[SWP: You suggested: I would say some-
42 thing about the dynamics of these pathogens not being well understood, but I've
43 since rewritten the most of intro and I'm not sure where I would fit this. If you have
44 any suggestions, let me know...]*

45 So far, the majority of epidemiological analyses of respiratory pathogens in the
46 context of the pandemic perturbations have focused on characterizing the timing of
47 rebound [1, 9, 5]. Instead, we seek to characterize how fast a pathogen returns to its
48 pre-pandemic dynamics. These two concepts have subtle but important differences:
49 for example, it took more than 3 years for human metapneumovirus to rebound in
50 Hong Kong but the observed epidemic patterns in 2024 are similar to pre-pandemic
51 seasonal means, suggesting a rapid return to pre-pandemic dynamics following a
52 perturbation (Figure 1). Measuring this rate of return is particularly useful because
53 it allows us to quantify the ecological resilience of a host-pathogen system [10, 11,
54 12, 13].

55 In this study, we lay out theoretical and statistical approaches to characterizing
56 the resilience of a host-pathogen system based on how fast the system recovers from
57 perturbation. We begin by laying out a few representative scenarios that capture
58 the potential impact of pandemic perturbations on endemic pathogen dynamics and
59 illustrate how resilience can be measured by comparing the pre- and post-pandemic
60 dynamics of susceptible and infected hosts. In practice, information on susceptible
61 hosts is often unavailable, making this theoretical approach infeasible. Instead, we
62 utilize a mathematical technique to reconstruct empirical attractors from the data
63 [14], which allows us to measure the rate at which the host-pathogen system ap-
64 proaches this empirical attractor after a perturbation; this rate corresponds to the
65 resilience of the host-pathogen system. We use this method to analyze pathogen
66 surveillance data for respiratory and non-respiratory pathogens from Canada, Hong
67 Kong, Korea, and US. Finally, we show that susceptible host dynamics explain vari-
68 ation in pathogen resilience.

69 Conceptual introduction to pathogen resilience

70 In classical ecological literature, resilience of an ecological system is measured by
71 the rate at which the system returns to its reference state following a perturbation
72 [10, 11, 12, 13]. This rate corresponds to the largest real part of the eigenvalues of

73 the linearized system near equilibrium—here, we refer to this value as the *intrinsic*
74 resilience of the system, which represents the expected rate of return from perturbed
75 states. In practice, we rarely know the true model describing population-level dy-
76 namics of common respiratory pathogens, limiting our ability to infer the intrinsic
77 resilience of a system. Instead, we can still measure the *empirical* resilience of a
78 host-pathogen system by looking at how fast the system returns to the pre-pandemic,
79 endemic dynamics after interventions are lifted.

80 As an example, we begin with a simple Susceptible-Infected-Recovered-Susceptible
81 (SIRS) model with seasonally forced transmission and demography (i.e., birth and
82 death). The SIRS model is the simplest model that allows for waning of immunity
83 and is commonly used for modeling the dynamics of respiratory pathogens [15]. First,
84 consider an intervention that reduce transmission by 50% for 6 months starting in
85 2020, which causes epidemic patterns to deviate from its original stable annual cycle
86 for a short period of time and eventually come back (Figure 2A). To measure the
87 resilience of this system empirically, we first need to be able to measure the dis-
88 tance from its pre-pandemic attractor. There are many ways we can measure the
89 distance from the attractor, but for illustrative purposes, we choose one of the most
90 parsimonious approach: that is, we look at how the susceptible (S) and infected (I)
91 populations change over time and measure the distance on the SI phase plane (Figure
92 2B). In this simple case, the locally estimated scatterplot smoothing (LOESS) fit in-
93 dicates that the distance from the attractor decreases exponentially (linearly on a log
94 scale) on average (Figure 2C). Furthermore, the overall rate of return approximates
95 the intrinsic resilience of the seasonally unforced system (Figure 2C).

96 Alternatively, pandemic perturbations can have a lasting impact on the pathogen
97 dynamics; as an example, we consider a scenario in which a 10% reduction in trans-
98 mission persists even after interevntions are lifted (Figure 2D–F). In such cases in
99 practice, we cannot know whether the pathogen will return to its original cycle or a
100 different cycle until many years have passed, and we cannot measure the distance to
101 the new unknown attractor that the system might eventually approach. Nonethe-
102 less, we can still measure the distance from the pre-pandemic attractor and ask
103 how the distance changes over time (Figure 2E). The LOESS fit suggests that the
104 distance from the pre-pandemic attractor will initially decrease exponentially on av-
105 erage (equivalently, linearly on a log scale) and eventually plateau (Figure 2F). Here,
106 a permanent 10% reduction in transmission rate slows the system, which causes the
107 distance from the pre-pandemic attractor initially to decrease at a slower rate (Figure
108 2F) than it would have otherwise (Figure 2C) before plateauing at a fixed distance
109 between the two attractors. This example shows that resilience is not necessarily an
110 intrinsic property of a specific pathogen. Instead, pathogen resilience is a property
111 of a specific attractor that a host-pathogen system approaches, which depends on
112 both pathogen and host characteristics.

113 Finally, transient phenomena can further complicate the picture (Figure 2G–I).
114 For example, a stage-structured model initially exhibits a stable annual cycle, but
115 perturbations from a 10% reduction in transmission for 6 months cause the epidemic

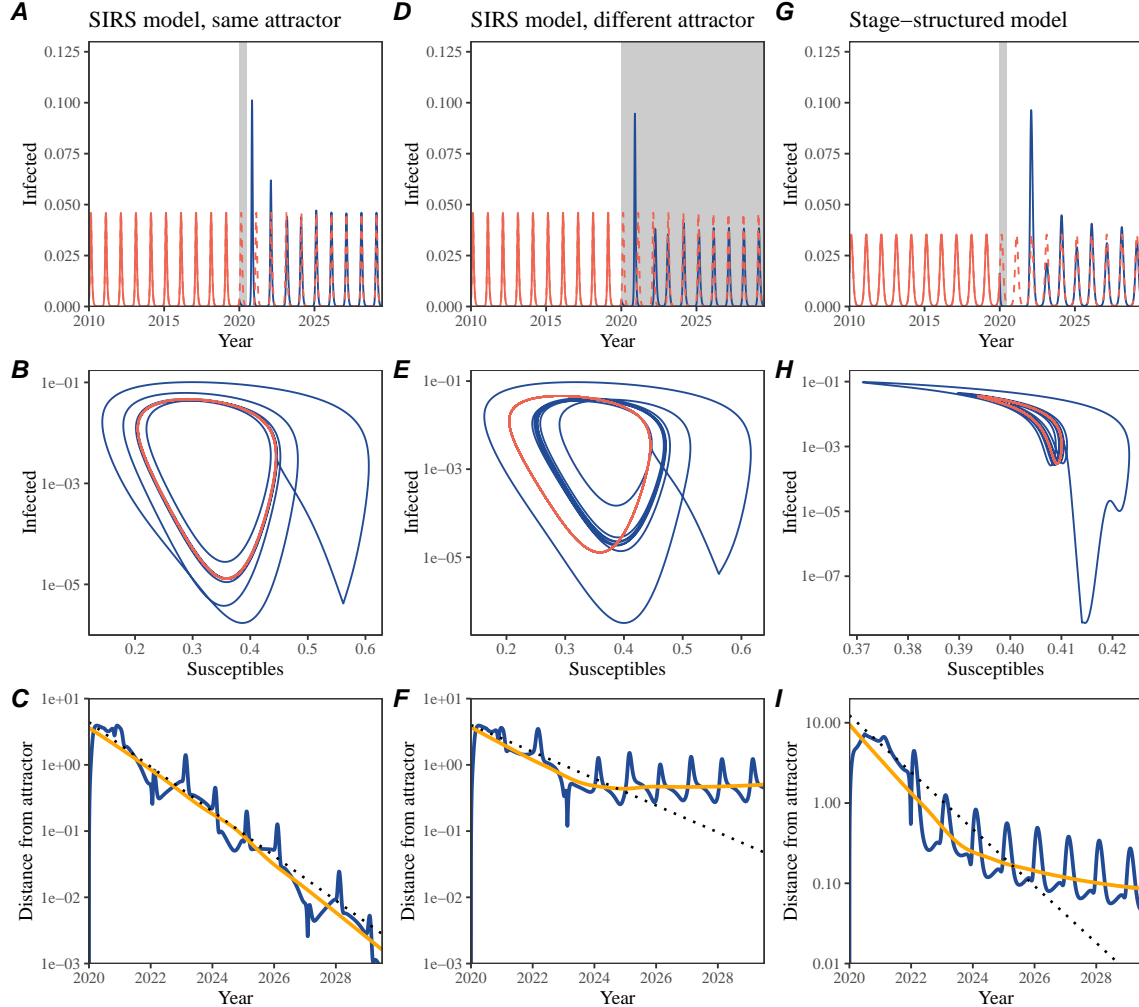


Figure 2: A simple method to measure pathogen resilience following pandemic perturbations across different scenarios. (A, D, G) Simulated epidemic trajectories across various models. Red and blue solid lines represent epidemic dynamics before and after interventions are introduced, respectively. Red dashed lines represent counterfactual epidemic dynamics in the absence of interventions. Gray regions indicate the duration of interventions. (B, E, H) Phase plane representation of the time series in panels A, D, and G alongside the corresponding susceptible host dynamics. Red and blue solid lines represent epidemic trajectories on an SI phase plane before and after interventions are introduced, respectively. (C, F, I) Changes in logged distance from the attractor over time. Blue lines represent the logged distance from the attractor. Orange lines represent the locally estimated scatterplot smoothing (LOESS) fits to the logged distance from the attractor. Dotted lines show the intrinsic resilience of the seasonally unforced system.

to shift to biennial cycles (Figure 2G). The system eventually approaches the original

117 pre-pandemic attractor (Figure 2H), suggesting that this biennial cycle is a transient
118 phenomenon. The LOESS fit indicates that the distance from the attractor initially
119 decreases exponentially at a rate that is consistent with the intrinsic resilience of
120 the seasonally unforced stage-structured system, but the rate of decrease decelerates
121 with the damped oscillations (Figure 2I). This behavior is also referred to as a ghost
122 attractor, which causes long transient dynamics and slow transitions [16]. Strong
123 seasonal forcing in transmission can also lead to transient phenomena for a simple
124 SIRS model, causing a slow return to pre-perturbation dynamics (Supplementary
125 Figure S1).

126 This empirical approach allows us to measure the resilience of a two-strain host-
127 pathogen system even when we have incomplete observation of the infection dynam-
128 ics. Simulations from a simple two-strain system illustrate that separate analyses of
129 individual strain dynamics (e.g., RSV A vs B) and a joint analysis of total infections
130 (e.g., total RSV infections) yield identical resilience estimates (Supplementary Fig-
131 ure S2, 3). This is expected because the dynamics of two strains (or two pathogens)
132 around the attractor in a coupled system are described by the same set of eigen-
133 values and eigenvectors, meaning that both strains should exhibit identical rates of
134 returns following a perturbation. Analogous to a single system, strong seasonal forc-
135 ing in transmission can cause the system to slow down through transient phenomena
136 (Supplementary Figure S4).

137 These observations indicate three possibilities. First, we can directly estimate the
138 empirical resilience of a host-pathogen system by measuring the rate at which the
139 system approaches an attractor, provided that we have a way to quantify the distance
140 from the attractor. The empirical approach to estimating pathogen resilience is
141 particularly convenient because it does not require us to know the true underlying
142 model; estimating the intrinsic resilience from fitting misspecified models can lead
143 to biased estimates (Supplementary Figure S5). Second, resilience estimates allow
144 us to make phenomenological predictions about the dynamics of a host-pathogen
145 system following a perturbation. Assuming that the distance from the attractor will
146 decrease exponentially over time, we can obtain a ballpark estimate for when the
147 system will reach an attractor; this prediction necessarily assumes that there won't
148 be permanent changes in pathogen dynamics (Figure 2F) or a long-term transient
149 phenomenon (Figure 2I). Finally, a change in the rate of an exponential decrease in
150 the distance from the attractor can provide information about whether the system
151 has reached an alternative attractor, or a ghost attractor, that is different from the
152 original, pre-pandemic attractor. These alternative attractors may reflect continued
153 perturbations from permanent changes in transmission patterns as well as changes in
154 immune landscapes. There will be periods of time when it is difficult to tell whether
155 pathogen dynamics are still diverging from its original attractor or have begun to
156 converge to an attractor; now that several years have passed since interventions have
157 been lifted, we expect many respiratory pathogens to have had sufficient time to
begin returning to their post-intervention attractors.

159 **Inferring pathogen resilience from real data**

160 Based on these observations, we now lay out our approach to estimating pathogen
161 resilience from real data (Figure 3). We then test this approach against simulations
162 and apply it to real data.

163 So far, we focused on simple examples that assume a constant transmission re-
164 duction. However, in practice, the impact of pandemic perturbations on pathogen
165 transmission is likely more complex (Figure 3A), reflecting introduction and relax-
166 ation of various intervention strategies. In some cases, strong perturbations can even
167 lead to a local fadeout, requiring immigration from another location for epidemic re-
168 emergence. These complexities can lead to longer delays between the introduction of
169 pandemic perturbations and pathogen re-emergence as well as temporal variation in
170 outbreak sizes (Figure 3B): in this example, continued transmission reduction from
171 interventions limits the size of the first outbreak in 2021 following the emergence,
172 allowing for a larger outbreak in 2022 when interventions are further relaxed.

173 Previously, we relied on the dynamics of susceptible and infected hosts to com-
174 pute the distance from the attractor (Figure 2), but information on susceptible hosts
175 is rarely available in practice. In addition, uncertainties in case counts due to obser-
176 vation error as well as multiannual cycles in the observed epidemic dynamics (e.g.,
177 adenovirus circulation patterns in Hong Kong and Korea) add challenges to defin-
178 ing pre-pandemic attractors, which limits our ability to measure the distance from
179 the attractor. To address these challenges, we can reconstruct an empirical attrac-
180 tor by utilizing Takens' theorem [14], which states that an attractor of a nonlinear
181 multidimensional system can be mapped onto a delayed embedding (Materials and
182 Methods). For example, we can use delayed logged values of pre-pandemic cases $C(t)$
183 (Figure 3C) to reconstruct the attractor:

$$\langle \log(C(t) + 1), \log(C(t - \tau) + 1), \dots, \log(C(t - (M - 1)\tau) + 1) \rangle, \quad (1)$$

184 where the delay τ and embedding dimension M are determined based on autocor-
185 relations and false nearest neighbors, respectively [17, 18]. We can then apply the
186 same delay and embedding dimensions to the entire time series to determine the
187 position on a multi-dimensional state space (Figure 3D), which allows us to mea-
188 sure the nearest neighbor distance between the current state of the system and the
189 empirical pre-pandemic attractor (Figure 3E). In theory, we can now quantify how
190 fast this distance decreases by fitting a linear regression on a log scale, where the
191 slope of the linear regression corresponds to pathogen resilience. However, resulting
192 estimates of pathogen resilience can be sensitive to choices about embedding delays
193 and dimensions; for example, using longer delays and higher dimensions tends to
194 smooth out temporal variations in the distance from the attractor (Supplementary
195 Figure S6).

196 Complex changes in the distance from the attractor suggest that estimating
197 pathogen resilience from linear regression will be particularly sensitive to our choice
198 of fitting windows for the regression (Figure 3E). Therefore, before we tried estimat-

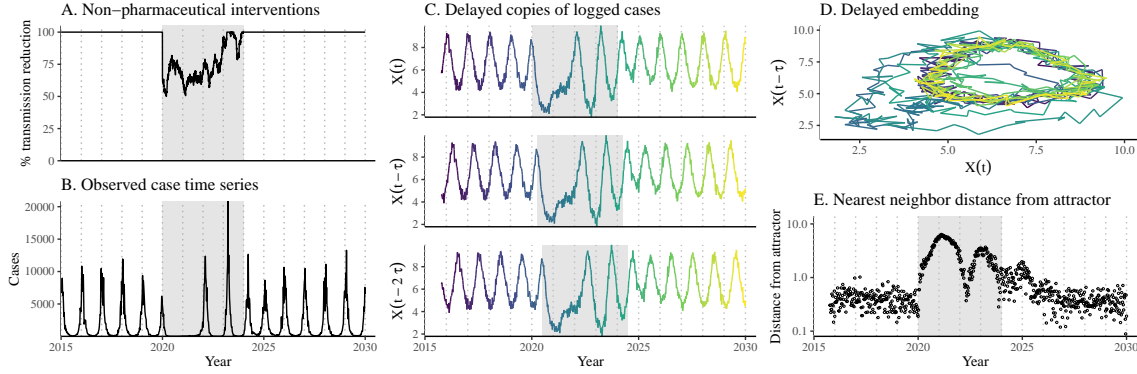


Figure 3: **A schematic diagram explaining the inference of pathogen resilience from synthetic data.** (A) A realistic example of simulated pandemic perturbations, represented by a relative reduction in transmission. (B) The impact of the synthetic pandemic perturbation on epidemic dynamics simulated using a SIRS model with demographic stochasticity. (C) Generating delayed copies of the logged time series allows us to obtain an embedding. (D) Two dimensional representation of an embedding. (E) Delayed embedding allows us to calculate the nearest neighbor distance from the empirical attractor, which is determined based on the pre-pandemic time series. This distance time series can be used to infer pathogen resilience after choosing an appropriate window for linear regression.

199 ing resilience from real data, we explored an automated window selection criterion
 200 for linear regression and test it against randomized, stochastic simulations across a
 201 wide range of realistic pandemic perturbation shapes; in doing so, we also explored
 202 optimal choices for embedding dimensions and evaluated our choices for fitting win-
 203 dows parameters and embedding dimensions by quantifying correlation coefficients
 204 between the estimated resilience and the intrinsic resilience of a seasonally unforced
 205 system (Materials and Methods). Overall, we find large variation in estimation
 206 performances with correlation coefficient ranging from 0.21 to 0.61 (Supplementary
 207 Figure S7). In almost all cases, the automated window selection approach outper-
 208 formed a naive approach that uses the entire time series, starting from the peak
 209 distance (Supplementary Figure S7).

210 Based on the best performing window selection criteria and embedding dimen-
 211 sion, we applied this approach to pathogen surveillance data presented in Figure
 212 1 (Materials and Methods). For each time series, we applied Takens' theorem in-
 213 dependently to reconstruct the empirical attractor and obtained the corresponding
 214 time series of distances from attractors (Supplementary Figure S8). Then, we use
 215 the automated window selection criterion to fit a linear regression and estimate the
 216 empirical resilience for each pathogen in each country (Supplementary Figure S8);
 217 the window selection criterion gave poor regression window for three cases (norovirus
 218 in Hong Kong and Korea and Rhinovirus/Enterovirus in the US), leading to unreal-
 219 istically low resilience estimates, and so we used ad-hoc regression windows instead

220 (Supplementary Figure S9; Materials and Methods).

221 For all pathogens we consider, resilience estimates fall between 0.4/year and
222 1.8/year (Figure 4A). We estimate the mean resilience of common respiratory pathogens
223 to be 0.99/year (95% CI: 0.80/year–1.18/year). As a reference, this is \approx 7.5 times
224 higher than the intrinsic resilience of pre-vaccination measles in England and Wales
225 (\approx 0.13/year). Finally, resilience estimates for norovirus are comparable to those of
226 common respiratory pathogens: 1.44/year (95%CI: 1.01/year–1.87/year) for Hong
227 Kong and 1.07/year (95%CI: 0.86/year–1.29/year) for Korea. Based on a simple
228 ANOVA test, we do not find significant differences in resilience estimates across
229 countries ($p = 0.25$) or pathogens ($p = 0.68$).

230 [SWP: You suggested “I think we probably need to spell out a bit more that
231 long-term changes in the transmission rate (or some other parameter) mean the at-
232 tractor is permanently different and the distance should remain nonzero” and I think
233 we’ve done that enough early on with current revisions so I don’t feel like we need
234 to do it again here. Let me know what you think.] Using resilience estimates, we
235 predicted when each pathogen would hypothetically return to their pre-pandemic
236 dynamics, assuming no long-term change in the attractor. Specifically, we extend
237 our linear regression fits to distance-from-attractor time series and ask when the pre-
238 dicted regression line will cross a threshold value; since we relied on nearest neighbor
239 distances, pre-pandemic distances are always greater than zero (Figure 3E), meaning
240 that we can use the mean of pre-pandemic distances as our threshold.

241 We predict that a return to pre-pandemic cycles would be imminent for most
242 pathogens (Figure 4B). In particular, we predict that 12 out of 23 pathogens should
243 have already returned before the end of 2024. For almost all pathogens that are
244 predicted to have returned already, the observed epidemic dynamics show clear con-
245 vergence towards their pre-pandemic seasonal averages, confirming our predictions
246 (Figure 4C). However, there are a few exceptions, including norovirus in Hong Kong
247 and Rhinovirus/Enterovirus in the US, where the observed epidemic dynamics in
248 2024 exhibit clear deviation from their pre-pandemic seasonal averages (Figure 4C).
249 These observations suggest a possibility that some common respiratory pathogens
250 may have converged to different attractors or are still exhibiting non-equilibrium
251 dynamics. In contrast, pathogens that are predicted to have not returned yet also
252 show clear differences from their pre-pandemic seasonal averages; as many of these
253 pathogens are predicted to return in 2025–2026, we may be able to test these pre-
254 dictions in near future (Supplementary Figure S10). Our reconstructions of distance
255 time series and estimates of pathogen resilience and expected return time are gener-
256 ally robust to choices of embedding dimensions (Supplementary Figure S11–12).

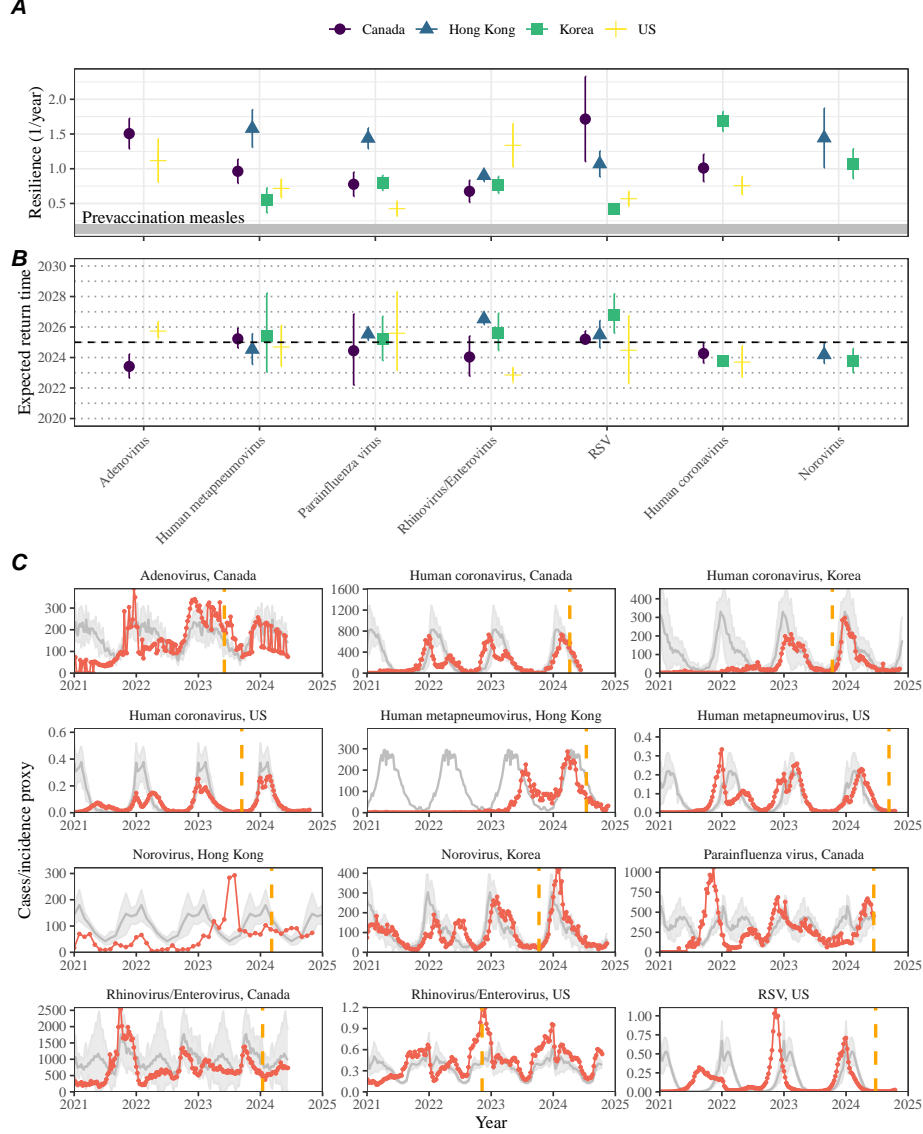


Figure 4: Summary of resilience estimates and predictions for return time. (A) Estimated pathogen resilience. The gray horizontal line represents the intrinsic resilience of pre-vaccination measles dynamics. (B) Predicted timing of when each pathogen will return to their pre-pandemic cycles. The dashed line in panel B indicates the end of 2024 (current observation time). Error bars represent 95% confidence intervals. (C) Observed dynamics for pathogen that are predicted to have returned before the end of 2024. Red points and lines represent data before 2020. Gray lines and shaded regions represent the mean seasonal patterns and corresponding 95% confidence intervals around the mean, previously shown in Figure 1. Orange vertical lines represent the predicted timing of return.

257 **Susceptible host dynamics explain variation in pathogen
258 resilience**

259 So far, we focused on quantifying pathogen resilience from the observed patterns
260 of pathogen re-emergence following pandemic perturbations. But what factors de-
261 termine how resilient a host-pathogen system is? Here, we use the SIRS model to
262 show that susceptible host dynamics are the key determinants of pathogen resilience.
263 To do so, we vary the basic reproduction number \mathcal{R}_0 , which represents the average
264 number of secondary infections caused by a newly infected individual in a fully sus-
265 ceptible population, and the duration of immunity and compute intrinsic resilience
266 for each parameter.

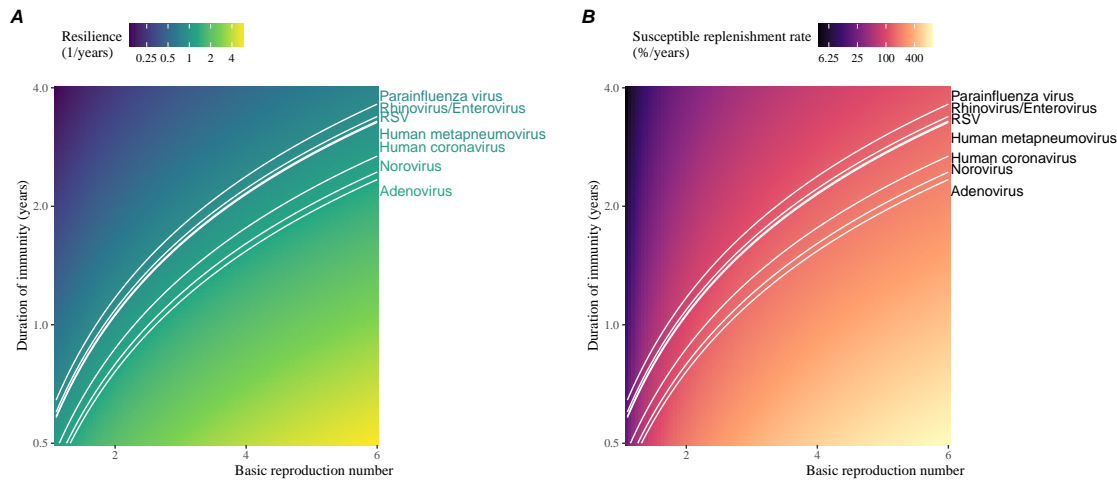


Figure 5: **Linking pathogen resilience to epidemiological parameters and susceptible host dynamics.** (A) The heat map represents intrinsic resilience as a function of the basic reproduction number \mathcal{R}_0 and the duration of immunity. (B) The heat map represents per-capita susceptible replenishment rate as a function of the basic reproduction number \mathcal{R}_0 and the duration of immunity. The standard SIRS model is used to compute intrinsic resilience and per-capita susceptible replenishment rate. Lines correspond to a set of parameters that are consistent with mean resilience estimates for each pathogen. Pathogens are ranked based on their mean resilience estimates, averaged across different countries.

267 We find an increase in \mathcal{R}_0 and a decrease in duration of immunity correspond
268 to an increase in pathogen resilience (Figure 5A). These variations can be under-
269 stood in terms of the susceptible host dynamics, where faster per-capita susceptible
270 replenishment rate causes the system to be more resilient (Figure 5B). This rate can
271 be expressed as a ratio between absolute rate at which new susceptibles enter the
272 population and the equilibrium number of susceptible individuals in the population,
273 \bar{S} . Therefore, both higher \mathcal{R}_0 and shorter duration of immunity can drive faster

274 per-capita susceptible replenishment rate (Figure 5B), especially because higher \mathcal{R}_0
275 leads to lower \bar{S} .

276 We can also rank different pathogens based on the average values of empirical
277 resilience computed previously, which allows us to determine a set of parameters that
278 are consistent with the estimated resilience (Figure 5A). Across all pathogens we
279 consider, except for bocavirus and norovirus, we estimate that the average duration
280 of immunity is likely to be short (< 4 years) across a plausible range of \mathcal{R}_0 (< 6).
281 These rankings further allow us to map each pathogen onto a set of SIRS parameters
282 that are consistent with its empirical resilience (Figure 5A) and obtain a plausible
283 range of susceptible replenishment rates for each pathogen (Figure 5B). However, we
284 note that there is no one-to-one correspondence between susceptible replenishment
285 rates and pathogen resilience, leading to a wide uncertainty in the estimates for
286 susceptible replenishment rates (Figure 5B).

287 **Pathogen resilience determines sensitivity to stochastic perturbations**

288

289 Beyond the pandemic perturbations, we expect host-pathogen systems to experience
290 continued perturbations of varying degrees from changes in epidemiological conditions,
291 such as human behavior, climate, and viral evolution. These perturbations
292 can also arise from demographic stochasticity, which is inherent to any ecological
293 systems. Here, we use a seasonally unforced SIRS model with birth/death to explore
294 how resilience of a host-pathogen system determines the sensitivity to perturbations
295 caused by demographic stochasticity (Materials and Methods).

296 We find that resilience of a host-pathogen system determines the amount of deviation
297 from the deterministic trajectory caused by demographic stochasticity, with less
298 resilient systems experiencing larger deviations (Figure 6). Notably, less resilience
299 systems also exhibit slower epidemic cycles; the periodicity of this epidemic cycle
300 matches those predicted by the intrinsic periodicity of the system (Supplementary
301 Figure S13). These conclusions are robust for the seasonally forced SIRS model
302 (Supplementary Figure S14),

303 **Discussion**

304 The pandemic interventions have caused major disruptions to circulation patterns of
305 both respiratory and non-respiratory pathogens, adding challenges to predicting their
306 future dynamics [1, 2, 3, 4]. However, these perturbations offer large-scale natural
307 experiments for understanding how different pathogens respond to perturbations. In
308 this study, we showed that pathogen re-emergence patterns following pandemic per-
309 turbations can be characterized through the lens of ecological resilience. We showed
310 that variation in pathogen resilience can be explained by the differences in suscepti-

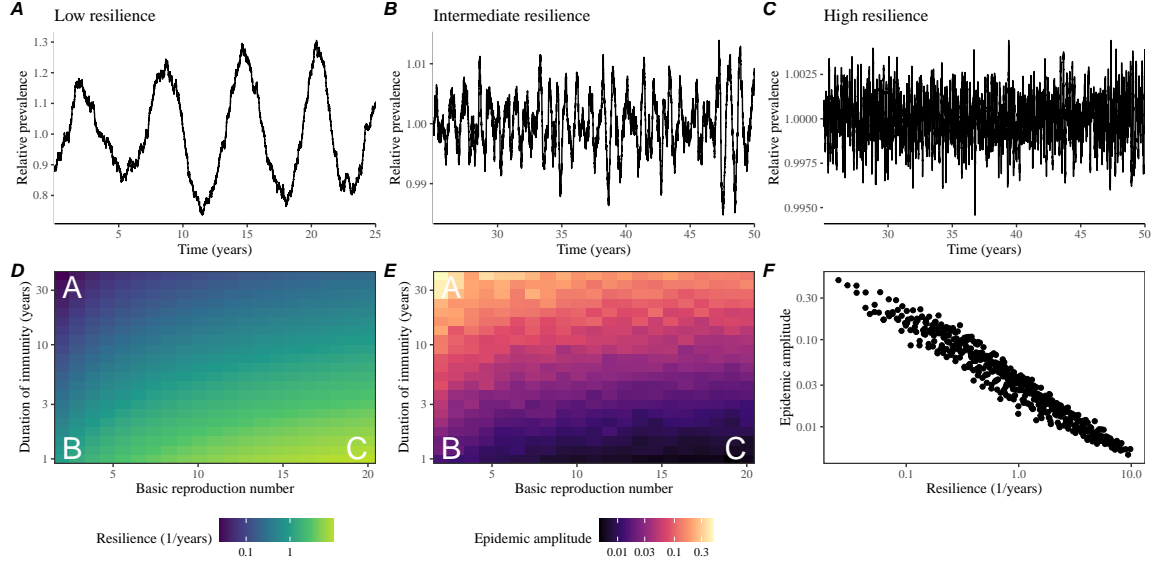


Figure 6: Linking resilience of a host-pathogen system to its sensitivity to stochastic perturbations. (A–C) Epidemic trajectories of a stochastic SIRS model across three different resilience values: low, intermediate, and high. The relative prevalence was calculated by dividing infection prevalence by its mean value. (D) The heat map represents the intrinsic resilience of a system as a function of the basic reproduction number \mathcal{R}_0 and the duration of immunity. (E) The heat map represents the epidemic amplitude as a function of the basic reproduction number \mathcal{R}_0 and the duration of immunity. The epidemic amplitude corresponds to $(\max I - \min I)/(2\bar{I})$, where \bar{I} represents the mean prevalence. (F) The relationship between pathogen resilience and epidemic amplitude.

311 ble host dynamics, where faster replenishment of the susceptible pool corresponds to
 312 a more resilient host-pathogen system. Finally, we showed that pathogen resilience
 313 also determines the sensitivity to stochastic perturbations.

314 We analyzed case time series of common respiratory infections and norovirus
 315 infections from Canada, Hong Kong, Korea, and the US to estimate their resilience.
 316 Overall, we estimated the resilience of these pathogens to range from 0.4/year to
 317 1.8/year, which is 3–14 times more resilient than prevaccination measles. These
 318 resilience estimates indicate that common respiratory pathogens and norovirus likely
 319 exhibit faster susceptible replenishment and are therefore more persistent, indicating
 320 potential challenges in controlling these pathogens.

321 Based on our resilience estimates, we made phenomenological predictions about
 322 when each pathogen will return to their endemic cycles. For the most part, we
 323 accurately predicted which pathogens should have already returned before the end
 324 of 2024. However, there were few exceptions (i.e., norovirus in Hong Kong and
 325 rhinovirus/enterovirus in the US), suggesting a possibility that these may have con-

326 verged to different endemic cycles compared to their pre-pandemic epidemic patterns.
327 These changes may reflect changes in surveillance or actual shift in the dynamics,
328 caused by permanent changes in behavior or population-level immunity. While it may
329 seem unlikely that permanent changes in behavior would only affect a few pathogens
330 and not others, we cannot rule out this possibility given heterogeneity in the age of
331 infection across different respiratory pathogens [19, 20]. Differences in the mode of
332 transmission between respiratory vs gastrointestinal pathogens may also contribute
333 to the differences in responses to pandemic perturbations. However, it is unclear
334 why norovirus dynamics in Korea seemed to have returned, whereas those in Hong
335 Kong have not.

336 For almost half of the pathogens we considered, we predicted that their return
337 to original epidemic patterns is imminent. We will need a few more years of data
338 to test whether these pathogens will eventually return to their original dynamics
339 or eventually converge to a different attractor. Overall, these observations echo
340 earlier studies that highlighted the long-lasting impact of pandemic perturbations
341 [8, 21, 22, 4].

342 We showed that susceptible host dynamics shape pathogen resilience, where faster
343 replenishment of the susceptible population causes the pathogen to be more resilient.
344 For simplicity, we focus on waning immunity and birth as the main drivers of the
345 susceptible host dynamics but other mechanisms can also contribute to the replen-
346 ishment of the susceptible population. In particular, pathogen evolution, especially
347 the emergence of antigenically novel strains, can cause effective waning of immunity
348 in the population; therefore, we hypothesize that faster rates of antigenic evolution
349 can also cause a pathogen to be more resilient. Future studies should explore the
350 relationship between the rate of evolution and resilience for antigenically evolving
351 pathogens.

352 Quantifying pathogen resilience also offers novel approaches to validating population-
353 level epidemiological models. So far, most of model validation in infectious disease
354 ecology is based on the ability of a model to reproduce the observed epidemic dy-
355 namics and to predict future dynamics [23, 24, 25, 26, 27]. However, many models
356 can perform similarly under these criteria. For example, two major RSV models
357 have been proposed to explain biennial epidemic patterns: (1) a stage- and age-
358 structured model that allows disease severity to vary with number of past infections
359 and age of infection [25] and (2) a pathogen-interaction model that accounts for cross
360 immunity between RSV and human metapneumovirus [24]. Since both models can
361 accurately reproduce the observed epidemic patterns, standard criteria for model
362 validation do not allow us to distinguish between these two models from population-
363 level data alone. Instead, it would be possible to measure the empirical resilience of
364 each model by simulating various perturbations and compare them to estimates of
365 empirical resilience from data, using pandemic NPIs as an opportunity.

366 There are several limitations to our work. First, we did not extensively explore
367 other approaches to reconstructing the attractor. Recent studies showed that more
368 sophisticated approaches, such as using non-uniform embedding, can provide more

robust reconstruction for noisy data [18]. In the context of causal inference, choices about embedding can have major impact on the resulting inference [28]. Our resilience estimates are likely overly confident given a lack of uncertainties in attractor reconstruction as well as the simplicity of our statistical framework. Nonetheless, as illustrated in our sensitivity analyses, inferences about pathogen resilience in our SIRS model appear to be robust to decisions about embedding lags and dimensions—this is because tracking the rate at which the system approaches the attractor is likely a much simpler problem than making inferences about causal directionality. Short pre-pandemic time series also limit our ability to accurately reconstruct the attractor and contribute to the crudeness of our resilience estimates; although this is less likely a problem for respiratory pathogens that are strongly annual, our attractor reconstruction may be inaccurate for those exhibiting multi-annual cycles, such as adenovirus in Hong Kong and Korea. Despite these limitations, our qualitative prediction that common respiratory pathogens are more resilient than prevaccination measles is also likely to be robust, given how rapid many respiratory pathogens returned to their original cycles following pandemic NPIs.

Predicting the impact of anthropogenic changes on infectious disease dynamics is a fundamental aim of infectious disease research in a rapidly changing world. Our study illustrates that quantifying pathogen resilience can help us understand how infectious disease pathogens respond to major perturbations caused by NPIs. More broadly, a detailed understanding of the determinants of pathogen resilience may offer unique insights into pathogen persistence and controllability.

Materials and Methods

Data

We gathered time series on respiratory infections from Canada, Hong Kong, Korea, and United States (US). As a reference, we also included time series data on norovirus infections for available countries. In contrast to respiratory pathogens, we expect gastrointestinal viruses, such as norovirus, to be differently affected by pandemic perturbations.

Weekly time series of respiratory infection cases in Canada comes from a publicly available website by the Respiratory Virus Detection Surveillance System, which collect data from select laboratories across Canada [29]. Weekly time series of respiratory infection cases in Hong Kong comes from a publicly available website by the Centre for Health Protection, Department of Health [30]. Weekly time series of acute respiratory infection cases in Korea comes from a publicly available website by the Korea Disease Control and Prevention Agency [31]. Finally, weekly time series of respiratory infection cases in the US were obtained from the National Respiratory and Enteric Virus Surveillance System. Time series on testing were also available in Canada, Hong Kong, and the US, but not in Korea. *[SWP: Not sure how to cite NREVSS data because we got it by emailing them...]*

409 **Data processing**

410 For all time series, we rounded every year to 52 weeks by taking the average number
411 of cases and tests between the 52nd and 53rd week. We also rescale all time series to
412 account for changes in testing patterns, which are then used for the actual analysis.

413 Canada: To account for an increase in testing from 2013 to 2024, we calculate
414 a 2 year moving average for the number of tests for each pathogen, which we use
415 as a proxy for testing effort. Then, we divide the smoothed testing patterns by the
416 smoothed value at the final week such that the testing effort has a maximum of 1.
417 We then divide weekly cases by the testing effort to obtain a scaled case time series.
418 A similar approach was used earlier for the analysis of RSV time series in the US
419 [25].

420 Hong Kong: We also apply the same scaling procedure to the time series as we did
421 for Canada. For Hong Kong, we only adjust for testing efforts up to the end of 2019
422 because there was a major reduction in testing for common respiratory pathogens
423 since 2020.

424 Korea: While we do not have information on testing, the reported number of
425 respiratory infections consistently increased from 2013 to the end of 2019, which we
426 interpreted as changes in testing patterns. Since we do not have testing numbers,
427 we used the weekly sum of all acute respiratory viral infection cases as a proxy for
428 testing, which were further smoothed with moving averaged and scaled to have a
429 maximum of 1. For Korea, we also only adjust for testing efforts up to the end of
430 2019.

431 US: In the US, there has been a large increase in testing against some respira-
432 tory pathogens, especially RSV, which could not be corrected for through simple
433 scaling. Instead, we derive an incidence proxy by multiplying the test positivity
434 with influenza-like illness positivity, which is taken from [https://gis.cdc.gov/
435 grasp/fluview/fluportaldashboard.html](https://gis.cdc.gov/grasp/fluview/fluportaldashboard.html). This method of estimating an inci-
436 dence proxy has been recently applied in the analysis of seasonal coronaviruses [7]
437 and *Mycoplasma pneumoniae* infections [4]. Detailed assumptions and justifications
438 are provided in [32].

439 **Estimating pathogen resilience**

440 In order to measure pathogen resilience from surveillance data, we first reconstruct
441 the empirical pre-pandemic attractor of the system using Takens' embedding theorem
442 [14]. Specifically, for a given pathogen, we take the pre-pandemic (before 2020)
443 case time series $C(t)$ and reconstruct the attractor using delayed embedding with a
444 uniform delay of τ and dimension M :

$$X_{\tau,m}(t) = \langle \log(C(t) + 1), \log(C(t - \tau) + 1), \dots, \log(C(t - (M - 1)\tau) + 1) \rangle. \quad (2)$$

445 Here, the delay τ is determined by calculating the autocorrelation of the logged pre-
446 pandemic time series and asking when the autocorrelation crosses 0 for the first time
447 [18]; a typical delay for an annual outbreak is around 13 weeks.

Then, for a given delay τ , we determine the embedding dimension M using the false nearest neighbors approach [17, 18]. To do so, we start with an embedding dimension e and construct a set of points $A_{\tau,e} = \{X_{\tau,e}(t) | t < 2020\}$. Then, for each point $X_{\tau,e}(t)$, we determine the nearest neighbor from the set $A_{\tau,e}$, which we denote $X_{\tau,e}(t_{nn})$ for $t \neq t_{nn}$. Then, if the distance between these two points on $e+1$ dimension, $D_{\tau,e+1}(t) = \|X_{\tau,e+1}(t_{nn}) - X_{\tau,e+1}(t)\|_2$, is larger than their distance on e dimension, $D_{\tau,e}(t) = \|X_{\tau,e}(t_{nn}) - X_{\tau,e}(t)\|_2$, these two points are deemed to be false nearest neighbors; specifically, we use a threshold R for the ratio between two distances $D_{\tau,e+1}(t)/D_{\tau,e}(t)$ to determine false nearest neighbors. In the main text, we determine the embedding dimension based on the first dimension without any false nearest neighbors for $R = 10$. In Supplementary Materials, we impose $R = 5$ to select for higher dimensions. Once we determine the embedding lag τ and dimension M , we apply the embedding to the entire time series and calculate the nearest neighbor distance against the attractor $A_{\tau,M}$ to obtain a time series of distance from the attractor $D_{\tau,M}(t)$.

From a time series of distances from the attractor, we estimate pathogen resilience by fitting a linear regression to an appropriate window. To automatically select the fitting window, we begin by smoothing the distance time series using locally estimated scatterplot smoothing (LOESS) to obtain $\hat{D}_{\tau,M}(t)$, where the smoothing is performed on a log scale and exponentiated afterwards. Then, we determine threshold values (T_{start} and T_{end}) for the smoothed distances and choose the fitting window based on when $\hat{D}_{\tau,M}(t)$ crosses these threshold values for the first time. These thresholds are determined by first calculating maximum distance,

$$\max \hat{D} = \max \hat{D}_{\tau,M}(t), \quad (3)$$

and mean pre-pandemic distance,

$$\hat{D}_{\text{mean}} = \frac{1}{N_{t<2020}} \sum_{t<2020} \hat{D}_{\tau,M}(t), \quad (4)$$

as a reference, and then dividing their ratios into 10 equal bins:

$$T_{\text{start}} = \hat{D}_{\text{mean}} \times \left(\frac{\max \hat{D}}{\hat{D}_{\text{mean}}} \right)^{9/10} \quad (5)$$

$$T_{\text{end}} = \hat{D}_{\text{mean}} \times \left(\frac{\max \hat{D}}{\hat{D}_{\text{mean}}} \right)^{1/10} \quad (6)$$

This allows us to discard the initial period during which the distance increases (from the introduction of intervention measures) and the final period during which the distance plateaus (as the system reaches an attractor). The fitting window is determined based on when the smoothed distance $\hat{D}_{\tau,M}(t)$ crosses these threshold values for the first time; then, we fit a linear regression to logged (unsmoothed) distances $\log D_{\tau,M}(t)$ using that window.

479 **Mathematical modeling**

480 Throughout the paper, we use a series of mathematical models to illustrate the con-
 481 cept of pathogen resilience and to understand the determinants of pathogen resilience.
 482 In general, the intrinsic resilience for a given system is given by the largest real part
 483 of the eigenvalues of the linearized system at endemic equilibrium. Here, we focus on
 484 the SIRS model with demography and present the details of other models in Supple-
 485 mentary Materials. The SIRS (Susceptible-Infected-Recovered-Susceptible) model is
 486 the simplest model that allows for waning of immunity, where recovered (immune)
 487 individuals are assumed to become fully susceptible after an average of $1/\delta$ time pe-
 488 riod. The dynamics of the SIRS model is described by the following set of differential
 489 equations:

$$\frac{dS}{dt} = \mu - \beta(t)SI - \mu S + \delta R \quad (7)$$

$$\frac{dI}{dt} = \beta(t)SI - (\gamma + \mu)I \quad (8)$$

$$\frac{dR}{dt} = \gamma I - (\delta + \mu)R \quad (9)$$

$$(10)$$

490 where μ represents the birth/death rate, $\beta(t)$ represents the time-varying trans-
 491 mission rate, and γ represents the recovery rate. The basic reproduction number
 492 $\mathcal{R}_0(t) = \beta(t)/(\gamma + \mu)$ is defined as the average number of secondary infections that
 493 a single infected individual would cause in a fully susceptible population at time t
 494 and measures the intrinsic transmissibility of a pathogen.

495 When we first introduce the idea of pathogen resilience (Figure 2), we impose
 496 sinusoidal changes to the transmission rate to account for seasonal transmission:

$$\beta(t) = b_1(1 + \theta \cos(2\pi(t - \phi)))\alpha(t), \quad (11)$$

497 where b_1 represents the baseline transmission rate, θ represents the seasonal am-
 498 plitude, and ϕ represents the seasonal offset term. Here, we also introduce an ex-
 499 tra multiplicative term $\alpha(t)$ to account for the impact of pandemic NPIs, where
 500 $\alpha(t) < 1$ indicates transmission reduction. Figure 2A and 2B are generated assum-
 501 ing $b_1 = 3 \times (365/7 + 1/50)/\text{years}$, $\theta = 0.2$, $\phi = 0$, $\mu = 1/50/\text{years}$, $\gamma = 365/7/\text{years}$,
 502 and $\delta = 1/2/\text{years}$. In Figure 2A, we impose a 50% transmission reduction for 6
 503 months from 2020:

$$\alpha(t) = \begin{cases} 0.5 & 2020 \leq t < 2020.5 \\ 1 & \text{otherwise} \end{cases} \quad (12)$$

504 In Figure 2B, we impose a 50% transmission reduction for 6 months from 2020 and
 505 a permanent 10% reduction onward:

$$\alpha(t) = \begin{cases} 1 & t < 2020 \\ 0.5 & 2020 \leq t < 2020.5 \\ 0.9 & 2020.5 \leq t \end{cases} \quad (13)$$

506 In both scenarios, we simulate the SIRS model from the following initial conditions
507 ($S(0) = 1/\mathcal{R}_0$, $I(0) = 1 \times 10^{-6}$, and $R(0) = 1 - S(0) - I(0)$) from 1900 until 2030.

508 To measure the empirical resilience of the SIR model (Figure 2C and 2F), we
509 compute the normalized distance between post-intervention susceptible and logged
510 infected proportions and their corresponding pre-intervention values at the same time
511 of year:

$$\sqrt{\left(\frac{S(t) - S_{\text{pre}}(t)}{\sigma_S}\right)^2 + \left(\frac{\log I(t) - \log I_{\text{pre}}(t)}{\sigma_{\log I}}\right)^2}, \quad (14)$$

512 where σ_S and $\sigma_{\log I}$ represent the standard deviation in the pre-intervention suscep-
513 tible and logged infected proportions. We normalize the differences in susceptible
514 and logged infected proportions to allow both quantities to equally contribute to the
515 changes in distance from the attractor. We used logged prevalence, instead of abso-
516 lute prevalence, in order to capture epidemic dynamics in deep troughs during the
517 intervention period. In Supplementary Materials, we also compare how the degree
518 of seasonal transmission affects empirical resilience by varying θ from 0 to 0.4; when
519 we assume no seasonality ($\theta = 0$), we do not normalize the distance because the
520 standard deviation of pre-intervention dynamics are zero.

521 Finally, we use the SIRS model to understand how underlying epidemiological
522 parameters affect pathogen resilience and link this relationship to underlying sus-
523 ceptible host dynamics. For the simple SIRS model without seasonal transmission
524 ($\theta = 0$), the intrinsic resilience corresponds to

$$-\frac{\text{Re}(\lambda)}{2} = \frac{\delta + \beta I^* + \mu}{2}. \quad (15)$$

525 Here, I^* represents the prevalence at endemic equilibrium:

$$I^* = \frac{(\delta + \mu)(\beta - (\gamma + \mu))}{\beta(\delta + \gamma + \mu)}. \quad (16)$$

526 The susceptible replenishment rate is given by

$$S_{\text{replenish}} = \frac{\mu + \delta R}{S^*}, \quad (17)$$

527 where $S^* = 1/\mathcal{R}_0$ represents the equilibrium proportion of susceptible individuals.
528 We vary the basic reproduction number \mathcal{R}_0 between 1.1 to 6 and the average duration
529 of immunity $1/\delta$ between 2 to 80 years, and compute these two quantities. In doing
530 so, we fix all other parameters: $\mu = 1/80/\text{years}$ and $\gamma = 365/7/\text{years}$.

531 Data availability

532 Funding

533 **Supplementary Text**

534 **Resilience of a stage-structured system.**

535 In Figure 2G–I, we use a more realistic, stage-structured model to illustrate how
 536 transient phenomena can cause the system to slow down. Specifically, we use the
 537 stage-structured RSV model proposed by [25], which assumes that subsequent rein-
 538 fections cause an individual to become less susceptible and transmissible than previ-
 539 ous infections. The model dynamics can be described as follows:

$$\frac{dM}{dt} = \mu - (\omega + \mu)M \quad (S1)$$

$$\frac{dS_0}{dt} = \omega M - (\lambda(t) + \mu)S_0 \quad (S2)$$

$$\frac{dI_1}{dt} = \lambda(t)S_0 - (\gamma_1 + \mu)I_1 \quad (S3)$$

$$\frac{dS_1}{dt} = \gamma_1 I_1 - (\sigma_1 \lambda(t) + \mu)S_1 \quad (S4)$$

$$\frac{dI_2}{dt} = \sigma_1 \lambda(t)S_1 - (\gamma_2 + \mu)I_2 \quad (S5)$$

$$\frac{dS_2}{dt} = \gamma_2 I_2 - (\sigma_2 \lambda(t) + \mu)S_2 \quad (S6)$$

$$\frac{dI_3}{dt} = \sigma_2 \lambda(t)S_2 - (\gamma_3 + \mu)I_3 \quad (S7)$$

$$\frac{dS_3}{dt} = \gamma_3 I_3 - (\sigma_3 \lambda(t) + \mu)S_3 + \gamma_4 I_4 \quad (S8)$$

$$\frac{dI_4}{dt} = \sigma_3 \lambda(t)S_3 - (\gamma_4 + \mu)I_4 \quad (S9)$$

(S10)

540 where M represents the proportion of individuals who are maternally immune; S_i
 541 represents the proportion of individuals who are susceptible after i prior infections; I_i
 542 represents the proportion of individuals who are currently (re)-infected with their i -th
 543 infection; μ represents the birth and death rates; $1/\omega$ represents the mean duration
 544 of maternal immunity; $1/\gamma_i$ represents the mean duration of infection; $\lambda(t)$ represents
 545 the force of infection; and σ_i represents the reduction in susceptibility for the i -th
 546 reinfection. The force of infection is modeled using a sinusoidal function:

$$\beta(t) = b_1(1 + \theta \cos(2\pi(t - \phi)))\alpha(t) \quad (S11)$$

$$\lambda(t) = \beta(I_1 + \rho_1 I_2 + \rho_2(I_3 + I_4)), \quad (S12)$$

547 where b_1 represents the baseline transmission rate; θ represents the seasonal ampli-
 548 tude; ϕ represents the seasonal offset term; $\alpha(t)$ represents the intervention effect;
 549 and ρ_i represents the impact of immunity on transmission reduction. We use the

following parameters to simulate the impact of interventions on epidemic dynamics [25]: $b_1 = 9 \times (365/10 + 1/80)/\text{years}$, $\theta = 0.2$, $\phi = -0.1$, $\omega = 365/112/\text{years}$, $\gamma_1 = 365/10/\text{years}$, $\gamma_2 = 365/7/\text{years}$, $\gamma_3 = 365/5/\text{years}$, $\sigma_1 = 0.76$, $\sigma_2 = 0.6$, $\sigma_3 = 0.4$, $\rho_1 = 0.75$, $\rho_2 = 0.51$, and $\mu = 1/80/\text{years}$. We assume a 50% transmission reduction for 6 months from 2020:

$$\alpha(t) = \begin{cases} 0.5 & 2020 \leq t < 2020.5 \\ 1 & \text{otherwise} \end{cases} \quad (\text{S13})$$

The model is simulated from 1900 to 2030 using the following initial conditions: $M = 0$, $S_0 = 1/\mathcal{R}_0 - I_1$, $I_1 = 1 \times 10^{-6}$, $S_1 = 1 - 1/\mathcal{R}_0$, $I_2 = 0$, $S_2 = 0$, $I_3 = 0$, $S_3 = 0$, and $I_4 = 0$. For the phase plane analysis (Figure 2H) and distance analysis (Figure 2I), we rely on the average susceptibility,

$$\bar{S} = S_0 + \sigma_1 S_1 + \sigma_2 S_2 + \sigma_3 S_3, \quad (\text{S14})$$

and total prevalence,

$$I_{\text{total}} = I_1 + I_2 + I_3 + I_4. \quad (\text{S15})$$

These quantities are used to compute the normalized distance from the attractor, as described in the main text.

Resilience of a multistrain system.

We use a simple two-strain model to show that a multistrain host-pathogen system that is coupled through cross immunity can be described by a single resilience value. The model dynamics can be described as follows [24]:

$$\frac{dS}{dt} = \mu - \mu S - (\lambda_1 + \lambda_2)S + \rho_1 R_1 + \rho_2 R_2 \quad (\text{S16})$$

$$\frac{dI_1}{dt} = \lambda_1 S - (\gamma_1 + \mu)I_1 \quad (\text{S17})$$

$$\frac{dI_2}{dt} = \lambda_2 S - (\gamma_2 + \mu)I_2 \quad (\text{S18})$$

$$\frac{dR_1}{dt} = \gamma_1 I_1 - \lambda_2 \epsilon_{21} R_1 - \rho_1 R_1 + \rho_2 R - \mu R_1 \quad (\text{S19})$$

$$\frac{dR_2}{dt} = \gamma_2 I_2 - \lambda_1 \epsilon_{12} R_2 - \rho_2 R_2 + \rho_1 R - \mu R_2 \quad (\text{S20})$$

$$\frac{dJ_1}{dt} = \lambda_1 \epsilon_{12} R_2 - (\gamma_1 + \mu)J_1 \quad (\text{S21})$$

$$\frac{dJ_2}{dt} = \lambda_2 \epsilon_{21} R_1 - (\gamma_2 + \mu)J_2 \quad (\text{S22})$$

$$\frac{dR}{dt} = \gamma_1 J_1 + \gamma_2 J_2 - \rho_1 R - \rho_2 R - \mu R \quad (\text{S23})$$

566 where S represents the proportion of individuals who are fully susceptible to infections
 567 by both strains; I_1 represents the proportion of individuals who are infected with strain 1 without prior immunity; I_2 represents the proportion of individuals who are infected with strain 2 without prior immunity; R_1 represents the proportion of individuals who are fully immune against strain 1 and partially susceptible to reinfection by strain 2; R_2 represents the proportion of individuals who are fully immune against strain 2 and partially susceptible to reinfection by strain 1; J_1 represents the proportion of individuals who are infected with strain 1 with prior immunity against strain 2; J_2 represents the proportion of individuals who are infected with strain 2 with prior immunity against strain 1; R represents the proportion of individuals who are immune to infections from both strains; μ represents the birth/death rate; λ_1 and λ_2 represent the force of infection from strains 1 and 2, respectively; ρ_1 and ρ_2 represent the waning immunity rate; γ_1 and γ_2 represent the recovery rate; ϵ_{21} and ϵ_{12} represent the susceptibility to reinfection with strains 2 and 1, respectively, given prior immunity from infection with strains 1 and 2, respectively. The force of infection is modeled as follows:

$$\beta_1 = b_1(1 + \theta_1 \sin(2\pi(t - \phi_1)))\alpha(t) \quad (\text{S24})$$

$$\beta_2 = b_2(1 + \theta_2 \sin(2\pi(t - \phi_2)))\alpha(t) \quad (\text{S25})$$

$$\lambda_1 = \beta_1(I_1 + J_1) \quad (\text{S26})$$

$$\lambda_2 = \beta_2(I_2 + J_2) \quad (\text{S27})$$

582 In Supplementary Figures S2–S4, we assume the following parameters: $b_1 = 2 \times$
 583 $52/\text{years}$, $b_2 = 4 \times 52/\text{years}$, $\phi_1 = \phi_2 = 0$, $\epsilon_{12} = 0.9$, $\epsilon_{21} = 0.5$, $\gamma_1 = \gamma_2 = 52/\text{years}$,
 584 $\rho_1 = \rho_2 = 1/\text{years}$, and $\mu = 1/70/\text{years}$. For all simulations, we assume a 50%
 585 transmission reduction for 6 months from 2020:

$$\alpha(t) = \begin{cases} 0.5 & 2020 \leq t < 2020.5 \\ 1 & \text{otherwise} \end{cases} \quad (\text{S28})$$

586 The seasonal amplitude θ is varied from 0 to 0.4. All simulations were ran from 1900
 587 to 2030 with following initial conditions: $S(0) = 1 - 2 \times 10^{-6}$, $I_1(0) = 1 \times 10^{-6}$,
 588 $I_2(0) = 1 \times 10^{-6}$, $R_1(0) = 0$, $R_2(0) = 0$, $J_1(0) = 0$, $J_2(0) = 0$, and $R(0) = 0$.

589 We consider three scenarios for measuring pathogen resilience: (1) we only have
 590 information about strain 1, (2) we only have information about strain 2, and (3)
 591 we are unable to distinguish between strains. In the first two scenarios (see panels
 592 A–C for strain 1 and panels D–F for strain 2), we consider the dynamics of average
 593 susceptibility for each strain and total prevalence:

$$\bar{S}_1 = S + \epsilon_{12}R_2 \quad (\text{S29})$$

$$\hat{I}_1 = I_1 + J_1 \quad (\text{S30})$$

$$\bar{S}_2 = S + \epsilon_{21}R_1 \quad (\text{S31})$$

$$\hat{I}_2 = I_2 + J_2 \quad (\text{S32})$$

⁵⁹⁴ In the third scenario (panels G–I), we consider the dynamics of total susceptible and
⁵⁹⁵ infected populations:

$$\hat{S} = S + R_2 + R_1 \quad (\text{S33})$$

$$\hat{I} = I_1 + J_1 + I_2 + J_2 \quad (\text{S34})$$

⁵⁹⁶ These quantities are used to compute the normalized distance from the attractor, as
⁵⁹⁷ described in the main text.

⁵⁹⁸ Estimating intrinsic resilience using mechanistic model

⁵⁹⁹ We tested whether we can reliably estimate the intrinsic resilience of a system by fit-
⁶⁰⁰ ting a mechanistic model. Specifically, we simulated case time series from stochastic
⁶⁰¹ SIRS and two-strain models and fitted a simple, deterministic SIRS model using a
⁶⁰² Bayesian framework.

⁶⁰³ We simulated the models in discrete time, incorporating demographic stochastic-
⁶⁰⁴ ity:

$$\beta(t) = \mathcal{R}_0 \left(1 + \theta \cos \left(\frac{2\pi t}{364} \right) \right) \alpha(t)(1 - \exp(-\gamma)) \quad (\text{S35})$$

$$\text{FOI}(t) = \beta(t)I(t - \Delta t)/N \quad (\text{S36})$$

$$B(t) \sim \text{Poisson}(\mu N) \quad (\text{S37})$$

$$\Delta S(t) \sim \text{Binom}(S(t - \Delta t), 1 - \exp(-(\text{FOI}(t) + \mu)\Delta t)) \quad (\text{S38})$$

$$N_{SI}(t) \sim \text{Binom}\left(\Delta S(t), \frac{\text{FOI}(t)}{\text{FOI}(t) + \mu}\right) \quad (\text{S39})$$

$$\Delta I(t) \sim \text{Binom}(I(t - \Delta t), 1 - \exp(-(\gamma + \mu)\Delta t)) \quad (\text{S40})$$

$$N_{IR}(t) \sim \text{Binom}\left(\Delta I(t), \frac{\gamma}{\gamma + \mu}\right) \quad (\text{S41})$$

$$\Delta R(t) \sim \text{Binom}(R(t - \Delta t), 1 - \exp(-(\delta + \mu)\Delta t)) \quad (\text{S42})$$

$$N_{RS}(t) \sim \text{Binom}\left(\Delta R(t), \frac{\delta}{\delta + \mu}\right) \quad (\text{S43})$$

$$S(t) = S(t - \Delta t) + N_{RS}(t) + B(t) - \Delta S(t) \quad (\text{S44})$$

$$I(t) = I(t - \Delta t) + N_{SI}(t) - \Delta I(t) \quad (\text{S45})$$

$$R(t) = R(t - \Delta t) + N_{IR}(t) - \Delta R(t) \quad (\text{S46})$$

⁶⁰⁵ where FOI represent the force of infection; N_{ij} represent the number of individuals
⁶⁰⁶ moving from compartment i to j on a given day; and $B(t)$ represents the number
⁶⁰⁷ of new births. We simulate the model on a daily scale—assuming 364 days in a
⁶⁰⁸ year so that it can be evenly grouped into 52 weeks—with the following parameters:
⁶⁰⁹ $\mathcal{R}_0 = 3$, $\theta = 0.1$, $\gamma = 1/7/\text{days}$, $\delta = 1/(364 \times 2)/\text{days}$, $\mu = 1/(364 \times 50)/\text{days}$, and
⁶¹⁰ $N = 1 \times 10^8$. The model is simulated from 1900 to 2030 assuming $S(0) = N/3$,

⁶¹¹ $I(0) = 100$, and $R(0) = N - S(0) - I(0)$. The observed incidence from the model is
⁶¹² then simulated as follows:

$$C(t) = \text{Beta-Binom}(N_{SI}(t), \rho, k), \quad (\text{S47})$$

⁶¹³ where ρ represents the reporting probability and k represents the overdispersion pa-
⁶¹⁴ rameter of beta-binomial distribution. Here, we use the beta-binomial distribution to
⁶¹⁵ account for overdispersion in reporting. We assume $\rho = 0.002$ (i.e., 0.2% probability)
⁶¹⁶ and $k = 1000$.

⁶¹⁷ We used an analogous approach for the two-strain model:

$$\beta_1(t) = b_1 \left(1 + \theta_1 \cos \left(\frac{2\pi(t - \phi_1)}{364} \right) \right) \alpha(t) \quad (\text{S48})$$

$$\beta_2(t) = b_2 \left(1 + \theta_2 \cos \left(\frac{2\pi(t - \phi_2)}{364} \right) \right) \alpha(t) \quad (\text{S49})$$

$$\text{FOI}_1(t) = \beta_1(t)(I_1(t - \Delta t) + J_1(t - \Delta t))/N \quad (\text{S50})$$

$$\text{FOI}_2(t) = \beta_2(t)(I_2(t - \Delta t) + J_2(t - \Delta t))/N \quad (\text{S51})$$

$$B(t) \sim \text{Poisson}(\mu N) \quad (\text{S52})$$

$$\Delta S(t) \sim \text{Binom}(S(t - \Delta t), 1 - \exp(-(\text{FOI}_1(t) + \text{FOI}_2(t) + \mu)\Delta t)) \quad (\text{S53})$$

$$N_{SI_1}(t) \sim \text{Binom}\left(\Delta S(t), \frac{\text{FOI}_1(t)}{\text{FOI}_1(t) + \text{FOI}_2(t) + \mu}\right) \quad (\text{S54})$$

$$N_{SI_2}(t) \sim \text{Binom}\left(\Delta S(t), \frac{\text{FOI}_2(t)}{\text{FOI}_1(t) + \text{FOI}_2(t) + \mu}\right) \quad (\text{S55})$$

$$\Delta I_1(t) \sim \text{Binom}(I_1(t - \Delta t), 1 - \exp(-(\gamma_1 + \mu)\Delta t)) \quad (\text{S56})$$

$$N_{I_1 R_1}(t) \sim \text{Binom}\left(\Delta I_1(t), \frac{\gamma_1}{\gamma_1 + \mu}\right) \quad (\text{S57})$$

$$\Delta I_2(t) \sim \text{Binom}(I_2(t - \Delta t), 1 - \exp(-(\gamma_2 + \mu)\Delta t)) \quad (\text{S58})$$

$$N_{I_2 R_2}(t) \sim \text{Binom}\left(\Delta I_2(t), \frac{\gamma_2}{\gamma_2 + \mu}\right) \quad (\text{S59})$$

$$\Delta R_1(t) \sim \text{Binom}(R_1(t - \Delta t), 1 - \exp(-(\epsilon_{21}\text{FOI}_2(t) + \rho_1 + \mu)\Delta t)) \quad (\text{S60})$$

$$N_{R_1 S}(t) \sim \text{Binom}\left(\Delta R_1(t), \frac{\rho_1}{\epsilon_{21}\text{FOI}_2(t) + \rho_1 + \mu}\right) \quad (\text{S61})$$

$$N_{R_1 J_2}(t) \sim \text{Binom}\left(\Delta R_1(t), \frac{\epsilon_{21}\text{FOI}_2(t)}{\epsilon_{21}\text{FOI}_2(t) + \rho_1 + \mu}\right) \quad (\text{S62})$$

$$\Delta R_2(t) \sim \text{Binom}(R_2(t - \Delta t), 1 - \exp(-(\epsilon_{12}\text{FOI}_1(t) + \rho_2 + \mu)\Delta t)) \quad (\text{S63})$$

$$N_{R_2 S}(t) \sim \text{Binom}\left(\Delta R_2(t), \frac{\rho_2}{\epsilon_{12}\text{FOI}_1(t) + \rho_2 + \mu}\right) \quad (\text{S64})$$

$$N_{R_2 J_1}(t) \sim \text{Binom}\left(\Delta R_2(t), \frac{\epsilon_{12}\text{FOI}_1(t)}{\epsilon_{12}\text{FOI}_1(t) + \rho_2 + \mu}\right) \quad (\text{S65})$$

$$\Delta J_1(t) \sim \text{Binom}(J_1(t - \Delta t), 1 - \exp(-(\gamma_1 + \mu)\Delta t)) \quad (\text{S66})$$

$$N_{J_1R}(t) \sim \text{Binom}\left(\Delta J_1(t), \frac{\gamma_1}{\gamma_1 + \mu}\right) \quad (\text{S67})$$

$$\Delta J_2(t) \sim \text{Binom}(J_2(t - \Delta t), 1 - \exp(-(\gamma_2 + \mu)\Delta t)) \quad (\text{S68})$$

$$N_{J_2R}(t) \sim \text{Binom}\left(\Delta J_2(t), \frac{\gamma_2}{\gamma_2 + \mu}\right) \quad (\text{S69})$$

$$\Delta R(t) \sim \text{Binom}(R(t - \Delta t), 1 - \exp(-(\rho_1 + \rho_2 + \mu)\Delta t)) \quad (\text{S70})$$

$$N_{RR_1}(t) \sim \text{Binom}\left(\Delta R(t), \frac{\rho_1}{\rho_1 + \rho_2 + \mu}\right) \quad (\text{S71})$$

$$N_{RR_2}(t) \sim \text{Binom}\left(\Delta R(t), \frac{\rho_2}{\rho_1 + \rho_2 + \mu}\right) \quad (\text{S72})$$

$$S(t) = S(t - \Delta t) - \Delta S(t) + B(t) + N_{R_1S}(t) + N_{R_2S}(t) \quad (\text{S73})$$

$$I_1(t) = I_1(t - \Delta t) - \Delta I_1(t) + N_{SI_1}(t) \quad (\text{S74})$$

$$I_2(t) = I_2(t - \Delta t) - \Delta I_2(t) + N_{SI_2}(t) \quad (\text{S75})$$

$$R_1(t) = R_1(t - \Delta t) - \Delta R_1(t) + N_{I_1R_1}(t) + N_{RR_1}(t) \quad (\text{S76})$$

$$R_2(t) = R_2(t - \Delta t) - \Delta R_2(t) + N_{I_2R_2}(t) + N_{RR_2}(t) \quad (\text{S77})$$

$$J_1(t) = J_1(t - \Delta t) - \Delta J_1(t) + N_{R_2J_1}(t) \quad (\text{S78})$$

$$J_2(t) = J_2(t - \Delta t) - \Delta J_2(t) + N_{R_1J_2}(t) \quad (\text{S79})$$

$$R(t) = R(t - \Delta t) - \Delta R(t) + N_{J_1R}(t) + N_{J_2R}(t) \quad (\text{S80})$$

618 We simulate the model on a daily scale with previously estimated parameters for the
 619 RSV-HMPV interaction [24]: $b_1 = 1.7/\text{weeks}$, $b_2 = 1.95/\text{weeks}$, $\theta_1 = 0.4$, $\theta_2 = 0.3$,
 620 $\phi_1 = 0.005 \times 7/364$, $\phi_2 = 4.99 \times 7/364$, $\epsilon_{12} = 0.92$, $\epsilon_{21} = 0.45$, $\gamma_1 = 1/10/\text{days}$,
 621 $\gamma_2 = 1/10/\text{days}$, $\rho_1 = 1/364/\text{days}$, $\rho_2 = 1/364/\text{days}$, $\mu = 1/(70 \times 364)/\text{days}$, and
 622 $N = 1 \times 10^8$. The model is simulated from 1900 to 2030 assuming $S(0) = N - 200$,
 623 $I_1(0) = 100$, $I_2(0) = 100$, $R_1(0) = 0$, $R_2(0) = 0$, $J_1(0) = 0$, $J_2(0) = 0$, and $R(0) = 0$.
 624 The observed incidence for each strain is then simulated as follows:

$$C_1(t) = \text{Beta} - \text{Binom}(N_{SI_1}(t) + N_{R_2J_1}, \rho, k), \quad (\text{S81})$$

$$C_2(t) = \text{Beta} - \text{Binom}(N_{SI_2}(t) + N_{R_1J_2}, \rho, k), \quad (\text{S82})$$

625 where ρ represents the reporting probability and k represents the overdispersion pa-
 626 rameter of beta-binomial distribution. We assume $\rho = 0.002$ (i.e., 0.2% probability)
 627 and $k = 500$. We also consider the total incidence: $C_{\text{total}}(t) = C_1(t) + C_2(t)$.

628 For both models, we consider a more realistic challenges in intervention effects
 629 $\alpha(t)$ to challenge our ability to estimate the intervention effects. Thus, we assume
 630 a 40% transmission reduction for 3 months from March 2020, followed by a 10%
 631 transmission reduction for 6 months, 20% transmission reduction for 3 months, and

632 a final return to normal levels:

$$\alpha(t) = \begin{cases} 1 & t < 2020.25 \\ 0.6 & 2020.25 \leq t < 2020.5 \\ 0.9 & 2020.5 \leq t < 2021 \\ 0.8 & 2021 \leq t < 2021.25 \\ 1 & 2021.25 \leq t \end{cases}. \quad (\text{S83})$$

633 For all simulations, we truncate the time series from the beginning of 2014 to the
634 end of 2023 and aggregate them into weekly cases.

635 To infer intrinsic resilience from time series, we fit a simple discrete time, deter-
636 ministic SIRS model [4]:

$$\Delta t = 1 \text{ week} \quad (\text{S84})$$

$$\text{FOI}(t) = \beta(t)(I(t - \Delta t) + \omega)/N \quad (\text{S85})$$

$$\Delta S(t) = [1 - \exp(-(\text{FOI}(t) + \mu)\Delta t)] S(t - \Delta t) \quad (\text{S86})$$

$$N_{SI}(t) = \frac{\text{FOI}(t)\Delta S(t)}{\text{FOI}(t) + \mu} \quad (\text{S87})$$

$$\Delta I(t) = [1 - \exp(-(\gamma + \mu)\Delta t)] I(t - \Delta t) \quad (\text{S88})$$

$$N_{IR}(t) = \frac{\gamma \Delta I(t)}{\gamma + \mu} \quad (\text{S89})$$

$$\Delta R(t) = [1 - \exp(-(\nu + \mu)\Delta t)] R(t - \Delta t) \quad (\text{S90})$$

$$N_{RS}(t) = \frac{\nu \Delta R(t)}{\nu + \mu} \quad (\text{S91})$$

$$S(t) = S(t - \Delta t) + \mu S - \Delta S(t) + N_{RS}(t) \quad (\text{S92})$$

$$I(t) = I(t - \Delta t) - \Delta I(t) + N_{SI}(t) \quad (\text{S93})$$

$$R(t) = R(t - \Delta t) - \Delta R(t) + N_{IR}(t) \quad (\text{S94})$$

637 where we include an extra term ω to account for external infections. Although actual
638 simulations do not include any external infections, we found that including this term
639 generally helped with model convergence in previous analyses [4]. The transmission
640 rate is divided into a seasonal term $\beta_{\text{seas}}(t)$ (repeated every year) and intervention
641 term $\alpha(t)$, which are estimated jointly:

$$\beta(t) = \beta_{\text{seas}}(t)\alpha(t), \quad (\text{S95})$$

642 where $\alpha < 1$ corresponds to reduction in transmission due to intervention effects. To
643 constrain the smoothness of $\beta_{\text{seas}}(t)$, we impose cyclic, random-walk priors:

$$\beta_{\text{seas}}(t) \sim \text{Normal}(\beta_{\text{seas}}(t - 1), \sigma) \quad t = 2 \dots 52 \quad (\text{S96})$$

$$\beta_{\text{seas}}(1) \sim \text{Normal}(\beta_{\text{seas}}(52), \sigma) \quad (\text{S97})$$

644 [SWP: I noticed that I forgot to put a prior on σ so need to re-do this but won't
 645 change the results.] We fix $\alpha(t) = 1$ for all $t < 2020$ and estimate α assuming a
 646 normal prior:

$$\alpha \sim \text{Normal}(1, 0.25). \quad (\text{S98})$$

647 We assume weakly informative priors on ω and ν :

$$\omega \sim \text{Normal}(0, 200) \quad (\text{S99})$$

$$\nu \sim \text{Normal}(104, 26) \quad (\text{S100})$$

648 We assume that the true birth/death rates, population sizes, and recovery rates are
 649 known. We note, however, that assuming $\gamma = 1/\text{week}$ actually corresponds to a
 650 mean simulated infectious period of 1.6 weeks, which is much longer than the true
 651 value; this approximation allows us to test whether we can still robustly estimate the
 652 intrinsic resilience given parameter mis-specification. Initial conditions are estimated
 653 with following priors:

$$S(0) = Ns(0) \quad (\text{S101})$$

$$I(0) = Ni(0) \quad (\text{S102})$$

$$s(0) \sim \text{Uniform}(0, 1) \quad (\text{S103})$$

$$i(0) \sim \text{Half-Normal}(0, 0.001) \quad (\text{S104})$$

654 Finally, the Observation model is specified as follows:

$$\text{Cases}(t) \sim \text{Negative-Binomial}(\rho N_{SI}(t), \phi) \quad (\text{S105})$$

$$\rho \sim \text{Half-Normal}(0, 0.02) \quad (\text{S106})$$

$$\phi \sim \text{Half-Normal}(0, 10) \quad (\text{S107})$$

655 where ρ represents the reporting probability and ϕ represents the negative binomial
 656 overdispersion parameter.

657 The model is fitted to four separate time series: (1) incidence time series from
 658 the SIRS model, (2) incidence time series for strain 1 from the two-strain model,
 659 (3) incidence time series for strain 2 from the two-strain model, and (4) combined
 660 incidence time series for strains 1 and 2 from the two-strain model. The model was
 661 fitted using rstan [33, 34]. The resulting posterior distribution was used to calculate
 662 the intrinsic resilience of the seasonally unforced system with the same parameters;
 663 eigenvalues of the discrete-time SIR model were computed by numerically finding
 664 the equilibrium and calculating the Jacobian matrix.

665 **Validations for window-selection criteria**

666 We use stochastic SIRS simulations to validate the window-selection criteria that we
 667 use for the linear regression for estimating empirical resilience. For each simulation,
 668 we begin by generating a random intervention $\alpha(t)$ from a random set of parameters.

669 First, we draw the duration of intervention τ_{npi} from a uniform distribution between
 670 0.5 and 3.5 years. Then, we draw independent normal variables z_i of length $\lfloor 364\tau_{\text{npi}} \rfloor$
 671 with a standard deviation of 0.02 and take a reverse cumulative sum to obtain a
 672 realistic shape for the intervention:

$$x_n = 1 + \sum_{i=n}^{\lfloor 364\tau_{\text{npi}} \rfloor} z_i, \quad n = 1, \dots, \lfloor 364\tau_{\text{npi}} \rfloor. \quad (\text{S108})$$

673 We repeat this random generation process until less than 10% of x_n exceeds 1. Then,
 674 we set any values that are above 1 or below 0 as 1 and 0, respectively. Then, we
 675 randomly draw the minimum transmission during intervention α_{\min} from a uniform
 676 distribution between 0.5 and 0.7 and scale x_n to have a minimum of α_{\min} :

$$x_{\text{scale},n} = \alpha_{\min} + (1 - \alpha_{\min}) \times \frac{x_n - \min x_n}{1 - \min x_n}. \quad (\text{S109})$$

677 This allows us to simulate a realistically shaped intervention:

$$\alpha(t) = \begin{cases} 1 & t < 2020 \\ x_{\text{scale},364(t-2020)} & 2020 \leq t < 2020 + \tau_{\text{npi}} \\ 1 & \tau_{\text{npi}} \leq t \end{cases}. \quad (\text{S110})$$

678 Given this intervention function, we draw \mathcal{R}_0 from a uniform distribution between 1.5
 679 and 3 and the mean duration of immunity $1/\delta$ from a uniform distribution between
 680 0.5 and 2. Then, we simulate the stochastic SIRS model from $S(0) = 10^8/\mathcal{R}_0$ and
 681 $I(0) = 100$ from 1990 to 2025 and truncate the time series to 2014–2025; if the
 682 epidemic becomes extinct before the end of simulation, we discard that simulation
 683 and start over from the intervention generation step. We then apply the window
 684 selection criteria described in the main text to compute the empirical resilience and
 685 compare it against the intrinsic resilience of the seasonally unforced system. We also
 686 compare this with the naive approach that uses the entire distance-from-attractor
 687 time series, starting from the maximum distance. We repeat this procedure 500
 688 times and quantify the correlation between empirical and intrinsic resilience estimates
 689 across two approaches.

690 Supplementary Figures

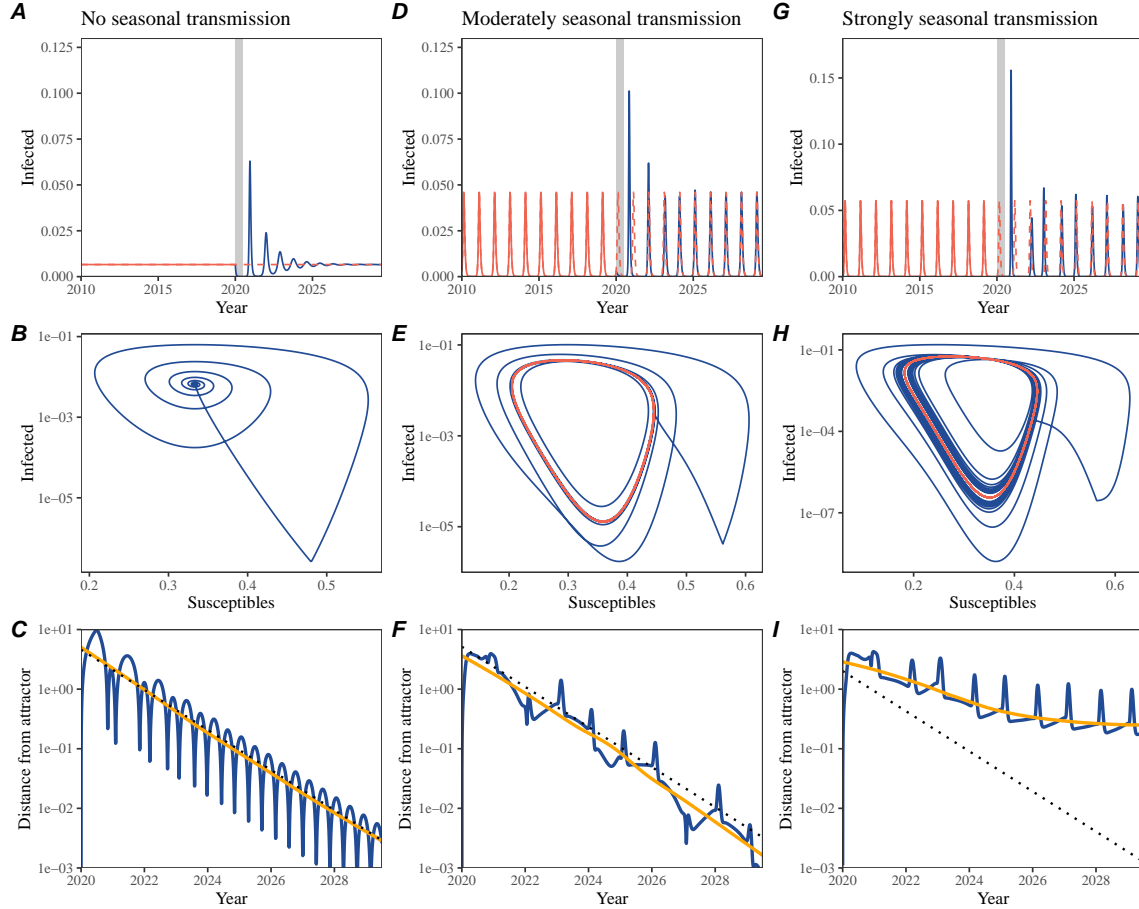


Figure S1: **Impact of seasonal transmission on pathogen resilience.** (A, D, G) Simulated epidemic trajectories using the SIRS model without seasonal forcing (A), with seasonal forcing of amplitude of 0.2 (D), and with seasonal forcing of amplitude of 0.4 (G). Red and blue solid lines represent epidemic dynamics before and after interventions are introduced, respectively. Red dashed lines represent counterfactual epidemic dynamics in the absence of interventions. Gray regions indicate the duration of interventions. (B, E, H) Phase plane representation of the corresponding model. Red and blue solid lines represent epidemic trajectories on an SI phase plane before and after interventions are introduced, respectively. (C, F, I) Changes in logged distance from the attractor over time. Blue lines represent the logged distance from the attractor. Orange lines represent the locally estimated scatterplot smoothing (LOESS) fits to the logged distance from the attractor. Dotted lines are superimposed as a comparison to have the same slope as the intrinsic resilience of the seasonally unforced system.

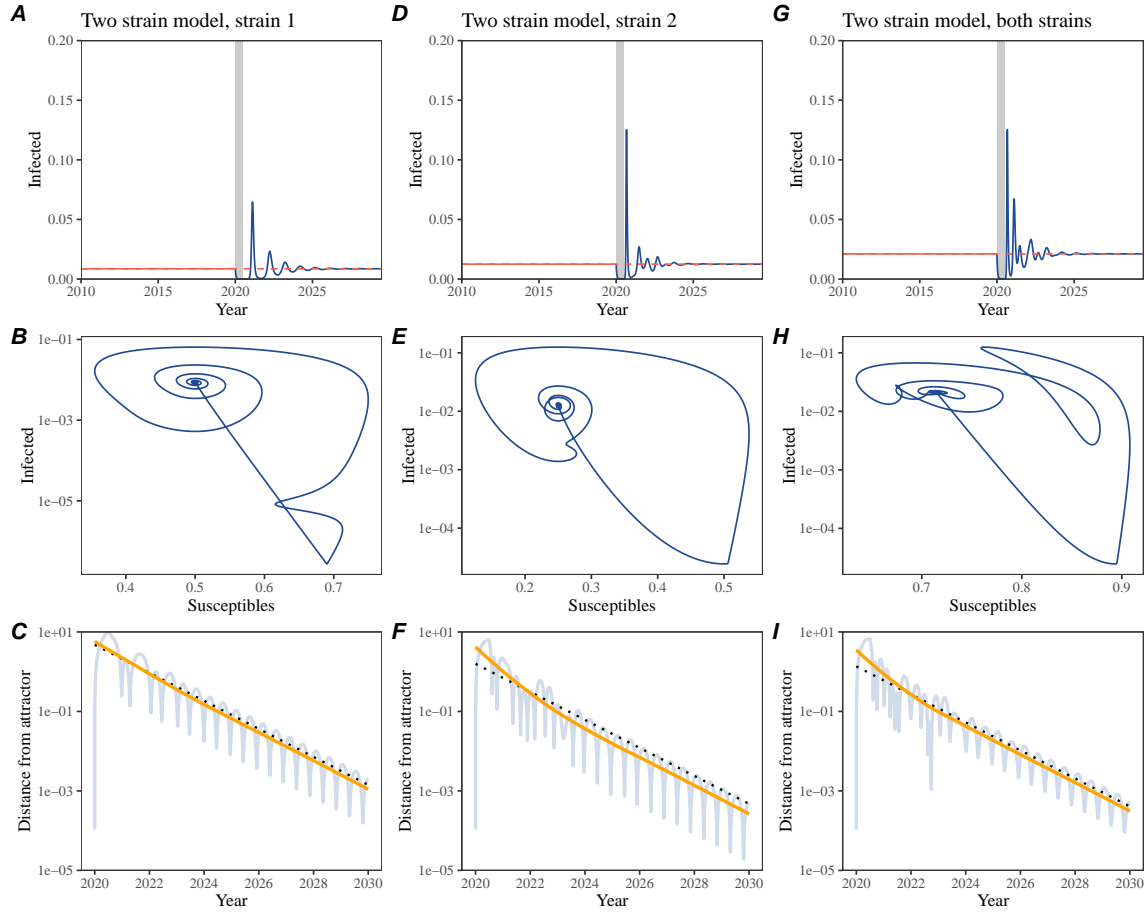


Figure S2: Conceptual framework for measuring pathogen resilience following NPIs for a two-strain system without seasonal forcing. (A, D, G) Simulated epidemic trajectories using a multi-strain system without seasonal forcing. Red and blue solid lines represent epidemic dynamics before and after interventions are introduced, respectively. Red dashed lines represent counterfactual epidemic dynamics in the absence of interventions. Gray regions indicate the duration of interventions. (B, E, H) Phase plane representation of the corresponding model. Blue solid lines represent epidemic trajectories on an SI phase plane before and after interventions are introduced, respectively. (C, F, I) Changes in logged distance from the attractor over time. Blue lines represent the logged distance from the attractor. Orange lines represent the locally estimated scatterplot smoothing (LOESS) fits to the logged distance from the attractor. Dotted lines are superimposed as a comparison to have the same slope as the intrinsic resilience of the seasonally unforced system.

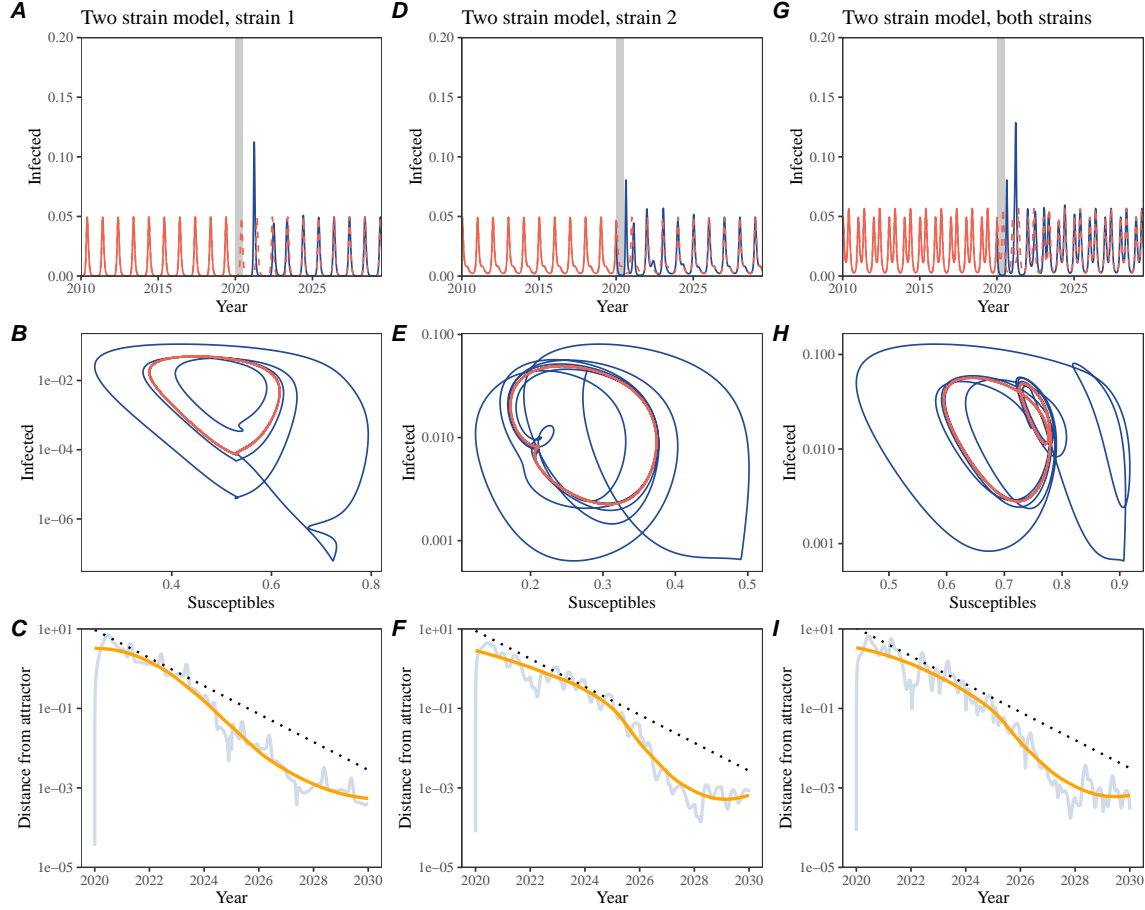


Figure S3: Conceptual framework for measuring pathogen resilience following NPIs for a multi-strain system with seasonal forcing. (A, D, G) Simulated epidemic trajectories using a multi-strain system with seasonal forcing (amplitude of 0.2). Red and blue solid lines represent epidemic dynamics before and after interventions are introduced, respectively. Red dashed lines represent counterfactual epidemic dynamics in the absence of interventions. Gray regions indicate the duration of interventions. (B, E, H) Phase plane representation of the corresponding model. Red and blue solid lines represent epidemic trajectories on an SI phase plane before and after interventions are introduced, respectively. (C, F, I) Changes in logged distance from the attractor over time. Blue lines represent the logged distance from the attractor. Orange lines represent the locally estimated scatterplot smoothing (LOESS) fits to the logged distance from the attractor. Dotted lines are superimposed as a comparison to have the same slope as the intrinsic resilience of the seasonally unforced system.

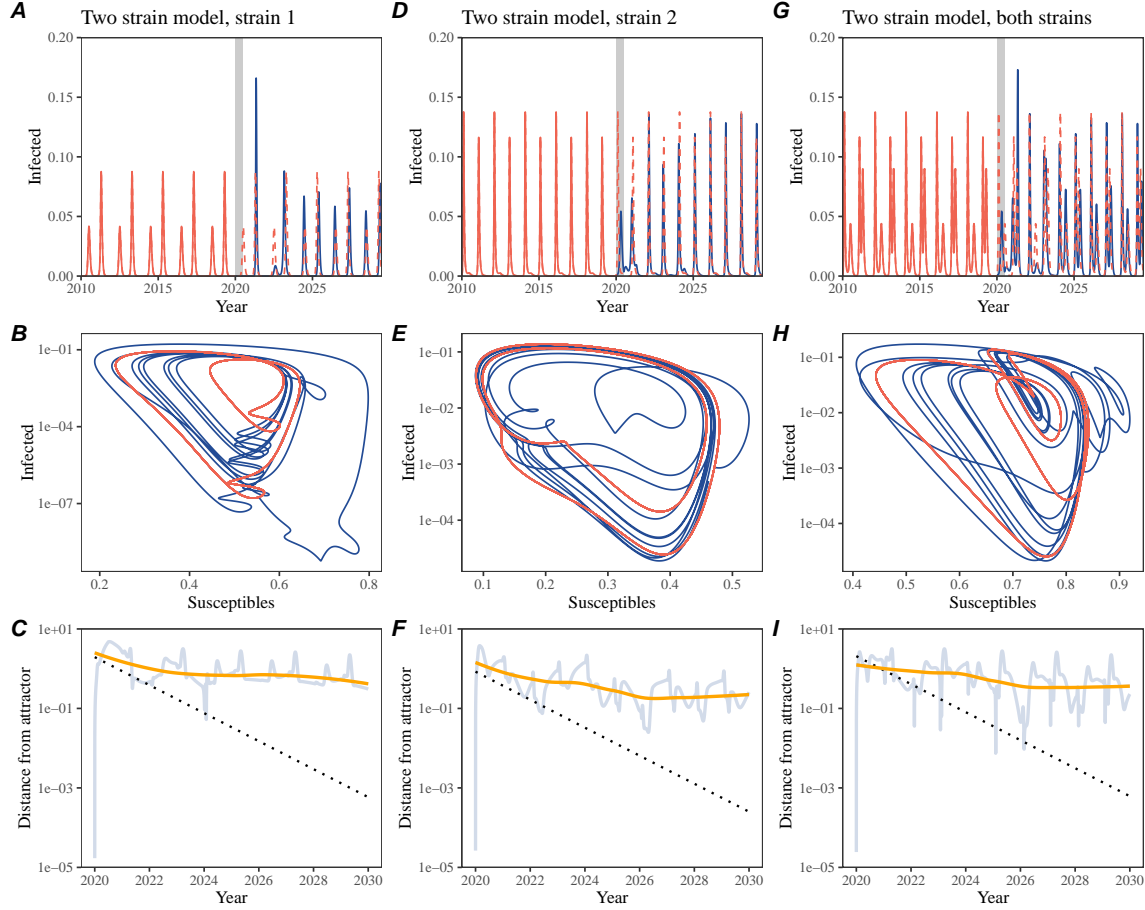


Figure S4: Conceptual framework for measuring pathogen resilience following NPIs for a multi-strain system with strong seasonal forcing. (A, D, G) Simulated epidemic trajectories using a multi-strain system with seasonal forcing (amplitude of 0.4). Red and blue solid lines represent epidemic dynamics before and after interventions are introduced, respectively. Red dashed lines represent counterfactual epidemic dynamics in the absence of interventions. Gray regions indicate the duration of interventions. (B, E, H) Phase plane representation of the corresponding model. Red and blue solid lines represent epidemic trajectories on an SI phase plane before and after interventions are introduced, respectively. (C, F, I) Changes in logged distance from the attractor over time. Blue lines represent the logged distance from the attractor. Orange lines represent the locally estimated scatterplot smoothing (LOESS) fits to the logged distance from the attractor. Dotted lines are superimposed as a comparison to have the same slope as the intrinsic resilience of the seasonally unforced system.

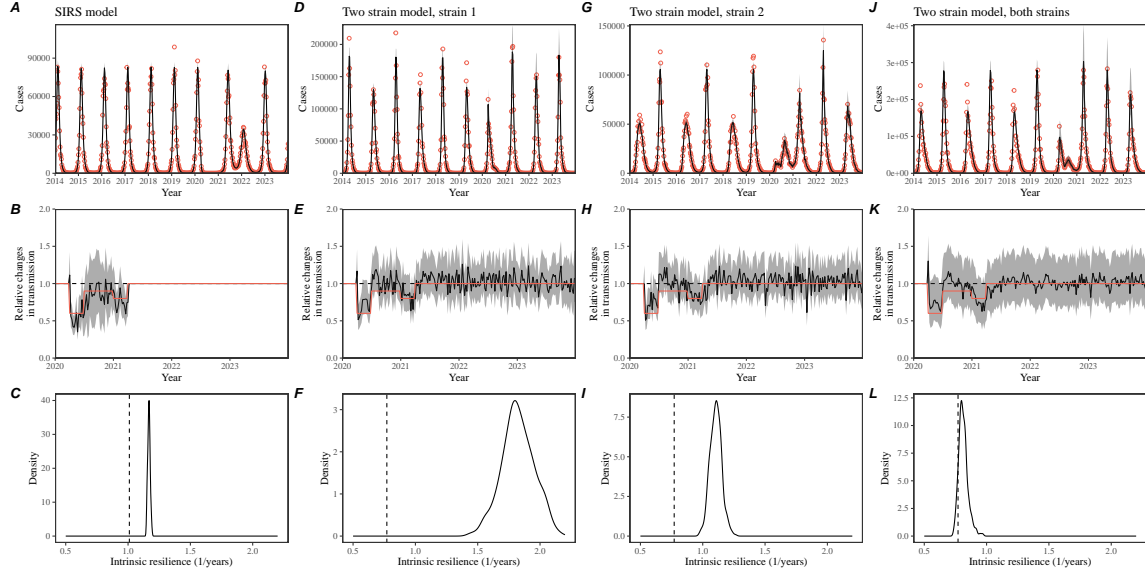


Figure S5: Mechanistic model fits to simulated data and inferred intrinsic resilience. (A, D, G, J) Simulated case time series from corresponding models (red) and SIRS model fits (black). (B, E, H, K) Assumed changes in transmission due to pandemic NPIs (red) and estimated changes from the SIRS model (black). Solid lines and shaded regions represent fitted posterior median and 95% credible intervals. (C, F, I, L) True intrinsic resilience of the seasonally unforced system (vertical lines) and the posterior distribution of the inferred intrinsic resilience from the SIRS model (density plots).

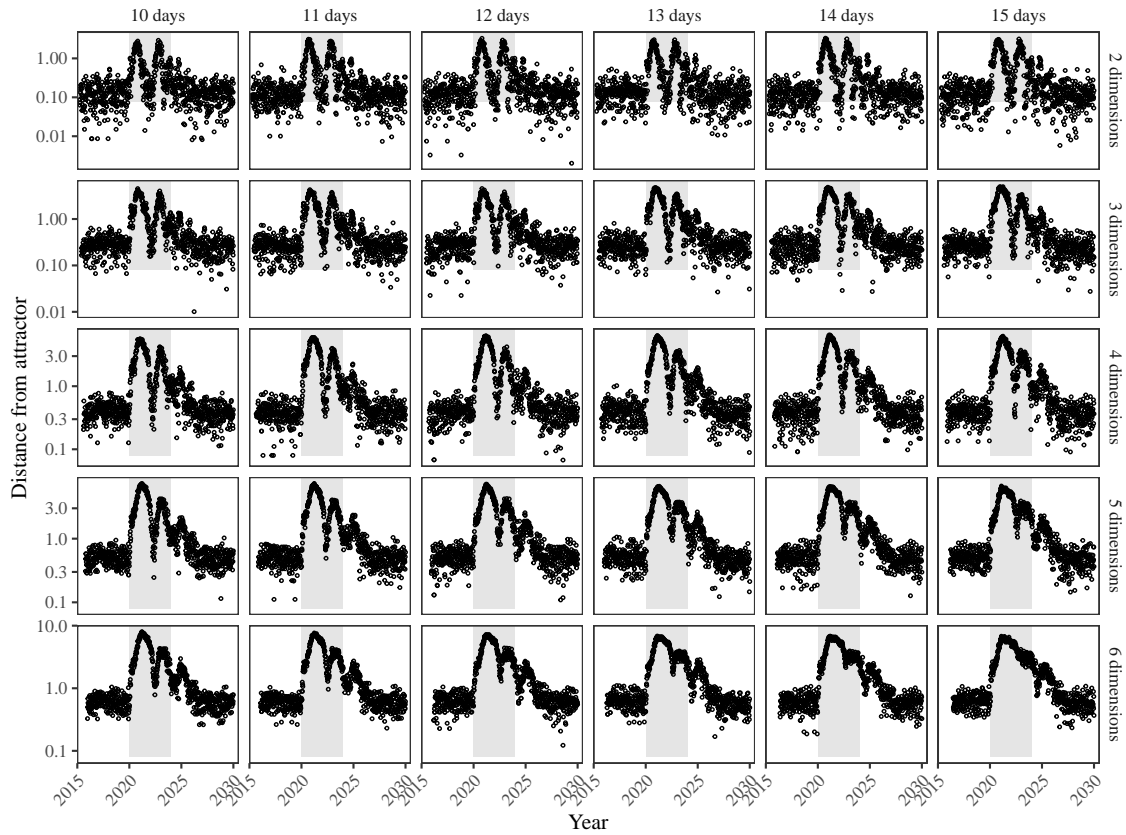


Figure S6: Sensitivity of the distance from the attractor to choices about embedding lags and dimensions. Sensitivity analysis for the distance-from-attractor time series shown in Figure 3E in the main text by varying the embedding lag between 10–15 days and embedding dimensions between 2–6 dimensions.

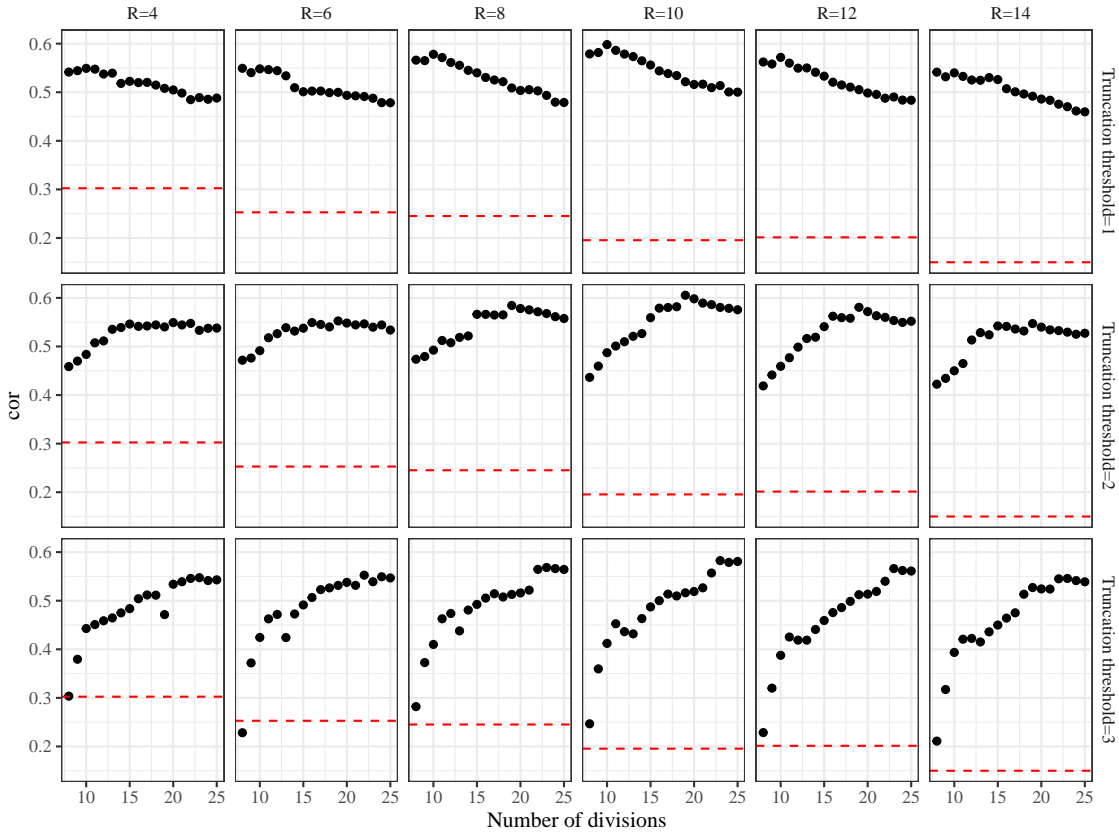


Figure S7: Impact of fitting window selection on the estimation of empirical resilience. We simulated 500 epidemics of a stochastic SIRS model with randomly drawn parameters and randomly generated intervention impacts. For each simulation, we reconstructed the empirical attractor based on the approach outlined in Figure 3 and estimate the distance from the attractor. The naive approach fits a linear regression on a log scale, starting from the maximum distance until the end of the time series. The window-based approach tries to select an appropriate window by smoothing the distance estimates and finding the time period when the smoothed time series crosses pre-determined threshold, relative to the maximum distance; then, a linear regression is fitted by using the raw distance within this time period.

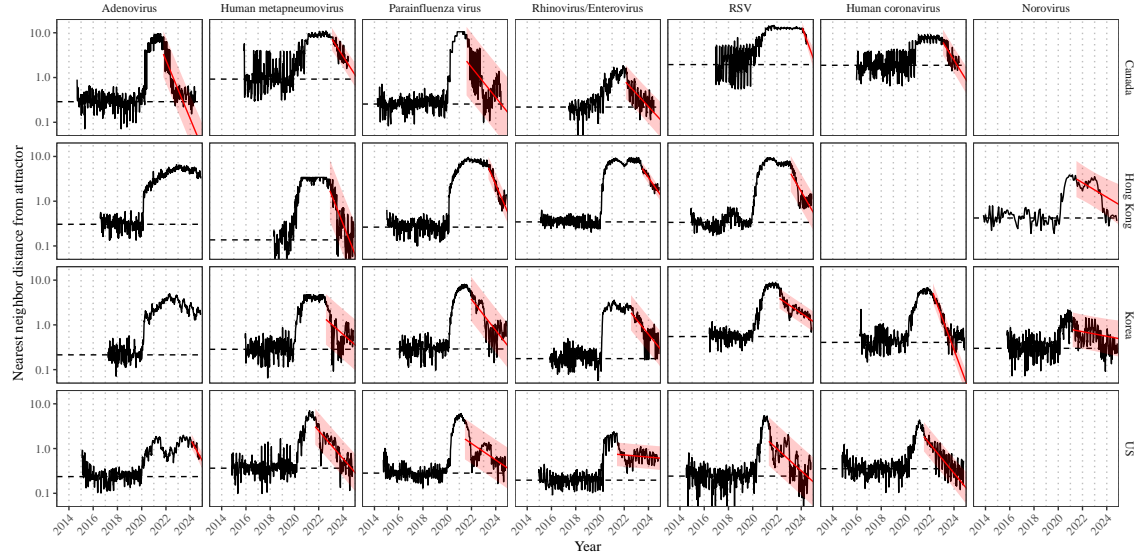


Figure S8: Estimated time series of distance from the attractor for each pathogen and corresponding linear regression fits using automated window selection criterion across Canada, Hong Kong, Korea, and the US. Black lines represent the estimated distance from the attractor. Red lines and shaded regions represent the linear regression fits and corresponding 95% confidence intervals. Dashed lines represent the average of the pre-pandemic nearest neighbor distances.

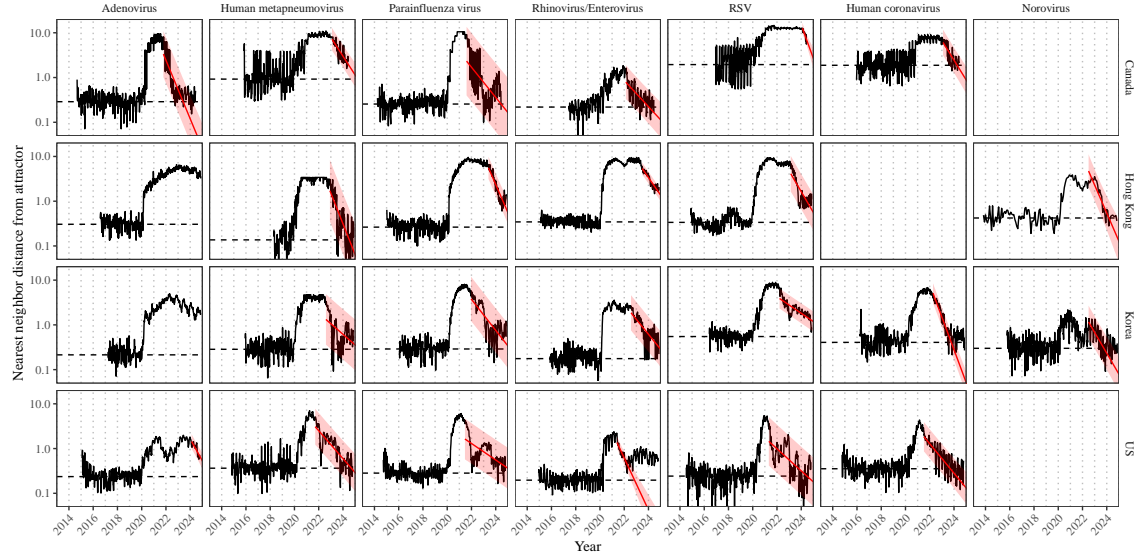


Figure S9: Estimated time series of distance from the attractor for each pathogen and corresponding linear regression fits across Canada, Hong Kong, Korea, and the US, including ad-hoc regression window selection. We used ad-hoc regression windows for norovirus in Hong Kong and Korea and Rhinovirus/Enterovirus in the US. Black lines represent the estimated distance from the attractor. Red lines and shaded regions represent the linear regression fits and corresponding 95% confidence intervals. Dashed lines represent the average of the pre-pandemic nearest neighbor distances.

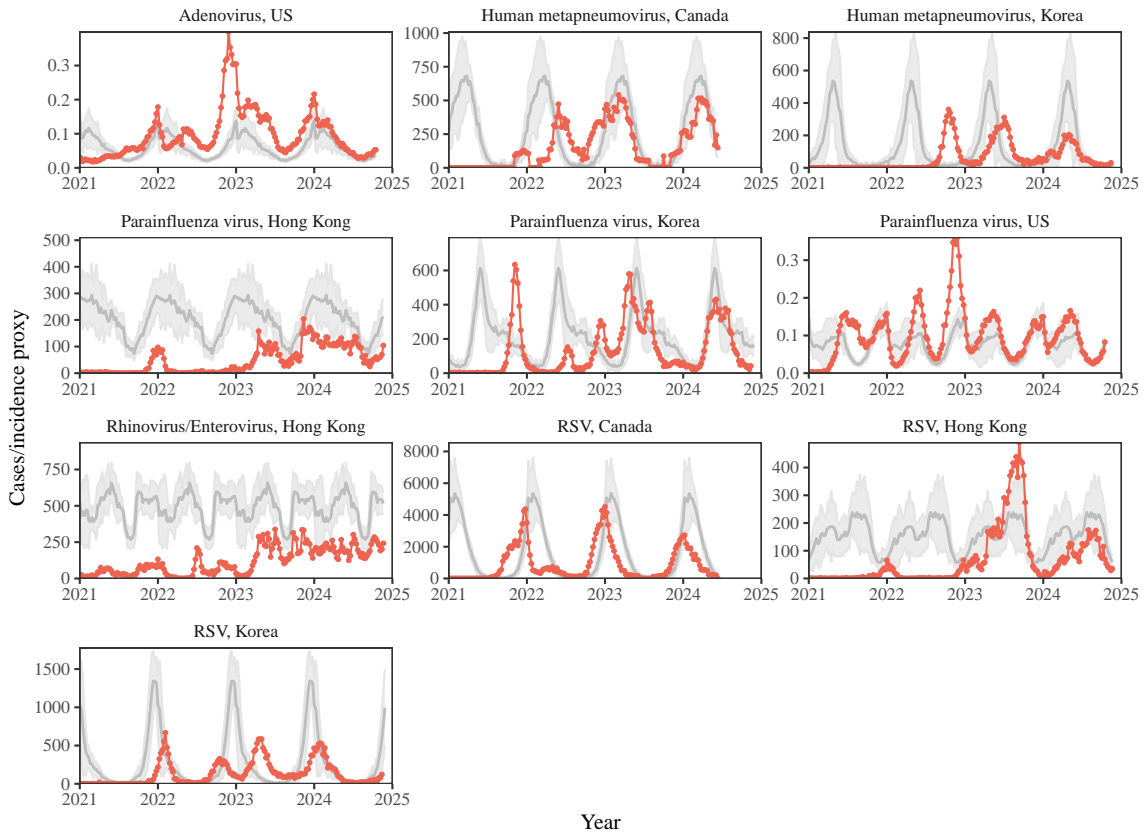


Figure S10: Observed dynamics for pathogen that are predicted to return after the end of 2024. Red points and lines represent data before 2020. Gray lines and shaded regions represent the mean seasonal patterns and corresponding 95% confidence intervals around the mean, previously shown in Figure 1.

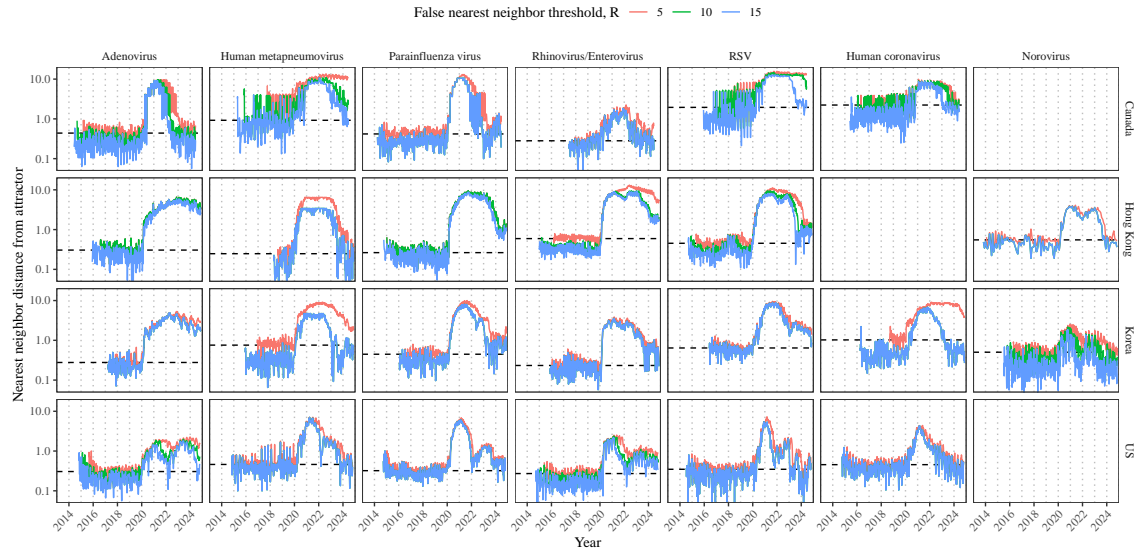


Figure S11: Estimated time series of distance from the attractor for each pathogen across different choices about false nearest neighbor threshold values. Using higher threshold values for the false nearest neighbor approach gives lower embedding dimensions. Colored lines represent the estimated distance from the attractor for different threshold values.

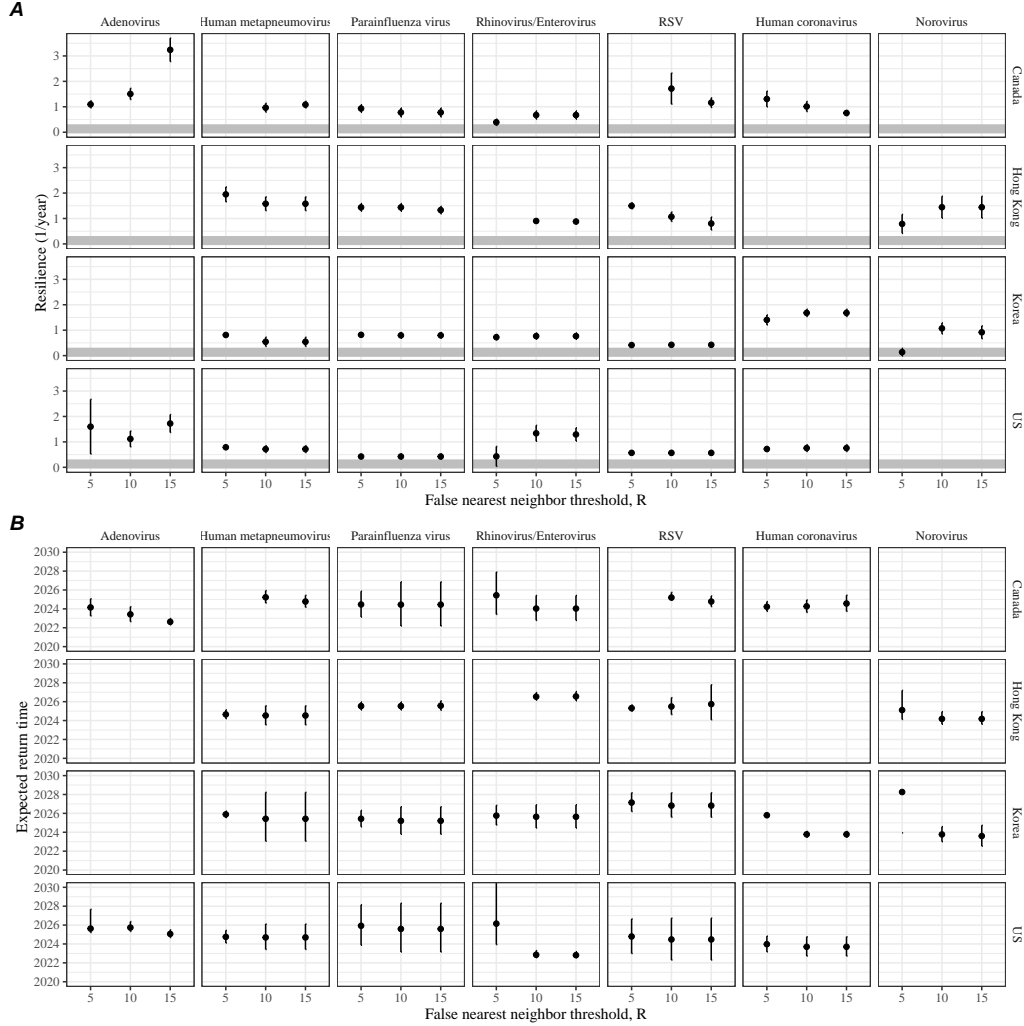


Figure S12: Summary of resilience estimates and predictions for return time across different choices about false nearest neighbor threshold values. The automated window selection method was used for all scenarios to estimate pathogen resilience, except for norovirus in Hong Kong and Korea and Rhinovirus/Enterovirus in the US. We used the same ad-hoc regression windows for norovirus in Hong Kong and Korea and Rhinovirus/Enterovirus in the US as we did in the main analysis. (A) Estimated pathogen resilience. The gray horizontal line represents the intrinsic resilience of pre-vaccination measles dynamics. (B) Predicted timing of when each pathogen will return to their pre-pandemic cycles. The dashed line in panel B indicates the end of 2024 (current observation time). Error bars represent 95% confidence intervals.

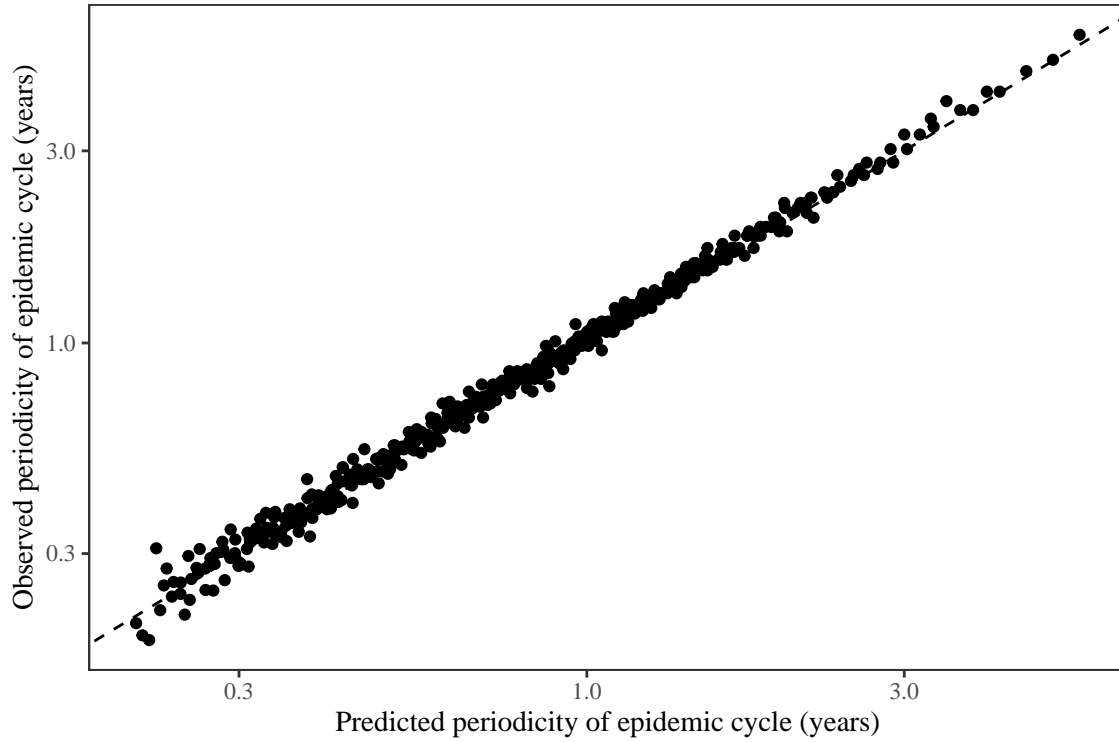


Figure S13: **Comparison between the observed and predicted periodicity of the epidemic cycle of the seasonally unforced SIRS model.** The observed periodicity of the epidemic corresponds to the periodicity at which maximum spectral density occurs. The predicted periodicity of the epidemic corresponds to $2\pi/\text{Im}(\lambda)$, where $\text{Im}(\lambda)$ is the imaginary part of the eigenvalue.

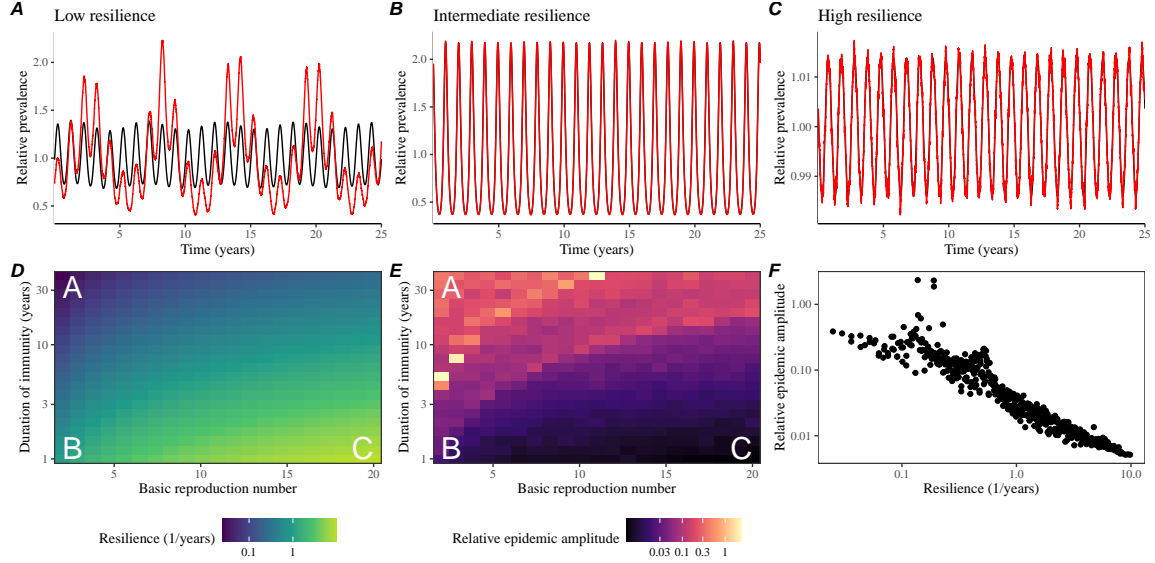


Figure S14: Linking resilience of a host-pathogen system to its sensitivity to stochastic perturbations for the seasonally forced SIRS model. (A–C) Epidemic trajectories of a stochastic SIRS model across three different resilience values: low, intermediate, and high. The relative prevalence was calculated by dividing infection prevalence by its mean value. (D) The heat map represents the intrinsic resilience of the seasonally unforced system as a function of the basic reproduction number \mathcal{R}_0 and the duration of immunity. (E) The heat map represents the relative epidemic amplitude as a function of the basic reproduction number \mathcal{R}_0 and the duration of immunity. To calculate the relative epidemic amplitude, we first take the relative difference in infection prevalence between stochastic and deterministic trajectories: $\epsilon = (I_{\text{stoch}} - I_{\text{det}})/I_{\text{det}}$. Then, we calculate the difference between maximum and minimum of the relative difference and divide by half: $(\max \epsilon - \min \epsilon)/2$. (F) The relationship between pathogen resilience and relative epidemic amplitude.

691 References

- 692 [1] Rachel E Baker, Sang Woo Park, Wenchang Yang, Gabriel A Vecchi, C Jessica E
693 Metcalf, and Bryan T Grenfell. The impact of COVID-19 nonpharmaceutical
694 interventions on the future dynamics of endemic infections. *Proceedings of the*
695 *National Academy of Sciences*, 117(48):30547–30553, 2020.
- 696 [2] Gabriela B Gomez, Cedric Mahé, and Sandra S Chaves. Uncertain effects of the
697 pandemic on respiratory viruses. *Science*, 372(6546):1043–1044, 2021.
- 698 [3] Mihaly Koltai, Fabienne Krauer, David Hodgson, Edwin van Leeuwen, Marina
699 Treskova-Schwarzbach, Mark Jit, and Stefan Flasche. Determinants of RSV
700 epidemiology following suppression through pandemic contact restrictions. *Epi-*
701 *demics*, 40:100614, 2022.
- 702 [4] Sang Woo Park, Brooklyn Noble, Emily Howerton, Bjarke F Nielsen, Sarah
703 Lentz, Lilliam Ambroggio, Samuel Dominguez, Kevin Messacar, and Bryan T
704 Grenfell. Predicting the impact of non-pharmaceutical interventions against
705 COVID-19 on *Mycoplasma pneumoniae* in the United States. *Epidemics*,
706 49:100808, 2024.
- 707 [5] Amanda C Perofsky, Chelsea L Hansen, Roy Burstein, Shanda Boyle, Robin
708 Prentice, Cooper Marshall, David Reinhart, Ben Capodanno, Melissa Truong,
709 Kristen Schwabe-Fry, et al. Impacts of human mobility on the citywide trans-
710 mission dynamics of 18 respiratory viruses in pre-and post-COVID-19 pandemic
711 years. *Nature communications*, 15(1):4164, 2024.
- 712 [6] Eric J Chow, Timothy M Uyeki, and Helen Y Chu. The effects of the COVID-19
713 pandemic on community respiratory virus activity. *Nature Reviews Microbiol-*
714 *ogy*, 21(3):195–210, 2023.
- 715 [7] Stephen M Kissler, Christine Tedijanto, Edward Goldstein, Yonatan H Grad,
716 and Marc Lipsitch. Projecting the transmission dynamics of SARS-CoV-2
717 through the postpandemic period. *Science*, 368(6493):860–868, 2020.
- 718 [8] Rachel E Baker, Chadi M Saad-Roy, Sang Woo Park, Jeremy Farrar, C Jessica E
719 Metcalf, and Bryan T Grenfell. Long-term benefits of nonpharmaceutical inter-
720 ventions for endemic infections are shaped by respiratory pathogen dynamics.
721 *Proceedings of the National Academy of Sciences*, 119(49):e2208895119, 2022.
- 722 [9] John-Sebastian Eden, Chisha Sikazwe, Ruopeng Xie, Yi-Mo Deng, Sheena G
723 Sullivan, Alice Michie, Avram Levy, Elena Cutmore, Christopher C Blyth,
724 Philip N Britton, et al. Off-season RSV epidemics in Australia after easing
725 of COVID-19 restrictions. *Nature communications*, 13(1):2884, 2022.
- 726 [10] Stuart L Pimm. The structure of food webs. *Theoretical population biology*,
727 16(2):144–158, 1979.

- 728 [11] Michael G Neubert and Hal Caswell. Alternatives to resilience for measuring
729 the responses of ecological systems to perturbations. *Ecology*, 78(3):653–665,
730 1997.
- 731 [12] Lance H Gunderson. Ecological resilience—in theory and application. *Annual
732 review of ecology and systematics*, 31(1):425–439, 2000.
- 733 [13] Vasilis Dakos and Sonia Kéfi. Ecological resilience: what to measure and how.
734 *Environmental Research Letters*, 17(4):043003, 2022.
- 735 [14] Floris Takens. Detecting strange attractors in turbulence. In *Dynamical Sys-
736 tems and Turbulence, Warwick 1980: proceedings of a symposium held at the
737 University of Warwick 1979/80*, pages 366–381. Springer, 2006.
- 738 [15] Jonathan Dushoff, Joshua B Plotkin, Simon A Levin, and David JD Earn. Dynamical resonance can account for seasonality of influenza epidemics. *Pro-
739 ceedings of the National Academy of Sciences*, 101(48):16915–16916, 2004.
- 741 [16] Alan Hastings, Karen C Abbott, Kim Cuddington, Tessa Francis, Gabriel Gell-
742 ner, Ying-Cheng Lai, Andrew Morozov, Sergei Petrovskii, Katherine Scran-
743 ton, and Mary Lou Zeeman. Transient phenomena in ecology. *Science*,
744 361(6406):eaat6412, 2018.
- 745 [17] Matthew B Kennel, Reggie Brown, and Henry DI Abarbanel. Determining
746 embedding dimension for phase-space reconstruction using a geometrical con-
747 struction. *Physical review A*, 45(6):3403, 1992.
- 748 [18] Eugene Tan, Shannon Algar, Débora Corrêa, Michael Small, Thomas Stemler,
749 and David Walker. Selecting embedding delays: An overview of embedding
750 techniques and a new method using persistent homology. *Chaos: An Interdis-
751 ciplinary Journal of Nonlinear Science*, 33(3), 2023.
- 752 [19] Jennifer M Radin, Anthony W Hawksworth, Peter E Kammerer, Melinda Bal-
753 ansay, Rema Raman, Suzanne P Lindsay, and Gary T Brice. Epidemiology
754 of pathogen-specific respiratory infections among three US populations. *PLoS
755 One*, 9(12):e114871, 2014.
- 756 [20] Guojian Lv, Limei Shi, Yi Liu, Xuecheng Sun, and Kai Mu. Epidemiological
757 characteristics of common respiratory pathogens in children. *Scientific Reports*,
758 14(1):16299, 2024.
- 759 [21] Saverio Caini, Adam Meijer, Marta C Nunes, Laetitia Henaff, Malaika Zounon,
760 Bronke Boudewijns, Marco Del Riccio, and John Paget. Probable extinction of
761 influenza b/yamagata and its public health implications: a systematic literature
762 review and assessment of global surveillance databases. *The Lancet Microbe*,
763 2024.

- 764 [22] Zhiyuan Chen, Joseph L-H Tsui, Bernardo Gutierrez, Simon Busch Moreno,
765 Louis du Plessis, Xiaowei Deng, Jun Cai, Sumali Bajaj, Marc A Suchard,
766 Oliver G Pybus, et al. COVID-19 pandemic interventions reshaped the global
767 dispersal of seasonal influenza viruses. *Science*, 386(6722):eadq3003, 2024.
- 768 [23] Bryan T Grenfell, Ottar N Bjørnstad, and Bärbel F Finkenstädt. Dynamics of
769 measles epidemics: scaling noise, determinism, and predictability with the TSIR
770 model. *Ecological monographs*, 72(2):185–202, 2002.
- 771 [24] Samit Bhattacharyya, Per H Gesteland, Kent Korgenski, Ottar N Bjørnstad,
772 and Frederick R Adler. Cross-immunity between strains explains the dynamical
773 pattern of paramyxoviruses. *Proceedings of the National Academy of Sciences*,
774 112(43):13396–13400, 2015.
- 775 [25] Virginia E Pitzer, Cécile Viboud, Wladimir J Alonso, Tanya Wilcox, C Jessica
776 Metcalf, Claudia A Steiner, Amber K Haynes, and Bryan T Grenfell. Environmental
777 drivers of the spatiotemporal dynamics of respiratory syncytial virus in
778 the United States. *PLoS pathogens*, 11(1):e1004591, 2015.
- 779 [26] Katharine R Dean, Fabienne Krauer, Lars Walløe, Ole Christian Lingjærde, Bar-
780 bara Bramanti, Nils Chr Stenseth, and Boris V Schmid. Human ectoparasites
781 and the spread of plague in Europe during the Second Pandemic. *Proceedings
782 of the National Academy of Sciences*, 115(6):1304–1309, 2018.
- 783 [27] Margarita Pons-Salort and Nicholas C Grassly. Serotype-specific immunity
784 explains the incidence of diseases caused by human enteroviruses. *Science*,
785 361(6404):800–803, 2018.
- 786 [28] Sarah Cobey and Edward B Baskerville. Limits to causal inference with state-
787 space reconstruction for infectious disease. *PloS one*, 11(12):e0169050, 2016.
- 788 [29] Public Health Agency of Canada. Respiratory virus detections in
789 Canada. 2024. <https://www.canada.ca/en/public-health/services/surveillance/respiratory-virus-detections-canada.html>. Accessed Sep
790 4, 2024.
- 792 [30] Centre for Health Protection. Detection of pathogens from respiratory
793 specimens. 2024. <https://www.canada.ca/en/public-health/services/surveillance/respiratory-virus-detections-canada.html>. Accessed Nov
794 20, 2024.
- 796 [31] Korea Disease Control and Prevention Agency. Acute respiratory infection,
797 Sentinel surveillance infectious diseases. 2024. <https://dportal.kdca.go.kr/pot/is/st/ari.do>. Accessed Nov 20, 2024.

- 799 [32] Edward Goldstein, Sarah Cobey, Saki Takahashi, Joel C Miller, and Marc Lipsitch. Predicting the epidemic sizes of influenza A/H1N1, A/H3N2, and B: a
800 statistical method. *PLoS medicine*, 8(7):e1001051, 2011.
- 801
- 802 [33] Bob Carpenter, Andrew Gelman, Matthew D Hoffman, Daniel Lee, Ben
803 Goodrich, Michael Betancourt, Marcus A Brubaker, Jiqiang Guo, Peter Li,
804 and Allen Riddell. Stan: A probabilistic programming language. *Journal of
805 statistical software*, 76, 2017.
- 806 [34] Stan Development Team. RStan: the R interface to Stan, 2024. R package
807 version 2.32.6.